eprints@whiterose.ac.uk
https://eprints.whiterose.ac.uk/

CrossMark

TREASUREHUNT: Transients and Variability Discovered with HST in the JWST North Ecliptic Pole Time-domain Field

Rosalia O'Brien[1], Rolf A. Jansen[1], Norman A. Grogin[2], Seth H. Cohen[1], Brent M. Smith[1], Ross M. Silver[3],
W. P. Maksym, III[4,5], Rogier A. Windhorst[1], Timothy Carleton[1], Anton M. Koekemoer[2], Nimish P. Hathi[2],
Christopher N. A. Willmer[6], Brenda L. Frye[6], M. Alpaslan[7], M. L. N. Ashby[4], T. A. Ashcraft[1,8], S. Bonoli[9,10],
W. Brisken[11], N. Cappelluti[12], F. Civano[3,4], C. J. Conselice[13], V. S. Dhillon[14,15], S. P. Driver[16], K. J. Duncan[17],
R. Dupke[18,19], M. Elvis[4], G. G. Fazio[4], S. L. Finkelstein[20], H. B. Gim[21], A. Griffiths[22], H. B. Hammel[23],
M. Hyun[24], M. Im[25], V. R. Jones[1], D. Kim[26], B. Ladjelate[27], R. L. Larson[20,28], S. Malhotra[3], M. A. Marshall[29,30],
S. N. Milam[31], J. D. R. Pierel[2], J. E. Rhoads[3], S. A. Rodney[32], H. J. A. Röttgering[33], M. J. Rutkowski[34],
R. E. Ryan, Jr.[2], M. J. Ward[35], C. W. White[1], R. J. van Weeren[33], X. Zhao[4], J. Summers[1], J. C. J. D'Silva[16,30],
R. Ortiz, III[1], A. S. G. Robotham[16], D. Coe[2,36,37], M. Nonino[38], N. Pirzkal[2], H. Yan[39], and T. Acharya[1]

[1] School of Earth and Space Exploration, Arizona State University, Tempe, AZ 85287-1404, USA; robrien5@asu.edu, rolf.jansen@asu.edu
[2] Space Telescope Science Institute, 3700 San Martin Drive, Baltimore, MD 21218, USA
[3] Astrophysics Science Division, NASA Goddard Space Flight Center, Greenbelt, MD 20771, USA
[4] Center for Astrophysics, Harvard & Smithsonian, Cambridge, MA 02138, USA
[5] NASA Marshall Space Flight Center, Huntsville, AL 35812, USA
[6] Department of Astronomy/Steward Observatory, University of Arizona, Tucson, AZ 85721, USA
[7] Center for Cosmology and Particle Physics, Department of Physics, New York University, NY 10003, USA
[8] Department of Physics, Eckerd College, St. Petersburg, FL 33711, USA
[9] Donostia International Physics Center, Paseo Manuel de Lardizabal 4, E-20118 Donostia-San Sebastián, Spain
[10] Ikerbasque, Basque Foundation for Science, E-48013 Bilbao, Spain
[11] National Radio Astronomy Observatory/Associated Universties, Inc., Charlottesville, VA 22903, USA
[12] Physics Department, University of Miami, Miami, FL 33124, USA
[13] Jodrell Bank Centre for Astrophysics, The University of Manchester, Manchester, M13 9PL, UK
[14] Department of Physics & Astronomy, The University of Sheffield, Sheffield, S3 7RH, UK
[15] Instituto de Astrofísica de Canarias, E-38205 La Laguna, Tenerife, Spain
[16] International Centre for Radio Astronomy Research, The University of Western Australia, Crawley, WA 6009, Australia
[17] Institute for Astronomy, The University of Edinburgh, Edinburgh, EH9 3HJ, UK
[18] Observatório Nacional, Rio de Janeiro, Brazil
[19] Eureka Scientific, Inc., Oakland, CA 94602, USA
[20] Department of Astronomy, The University of Texas at Austin, Austin, TX 78712, USA
[21] Department of Physics, Montana State University, Bozeman, MT 59717, USA
[22] School of Physics and Astronomy, The University of Nottingham, Nottingham, NG7 2RD, UK
[23] Association of Universities for Research in Astronomy, Washington, DC 20004, USA
[24] Korea Astronomy and Space Science Institute, Yuseong-gu, Daejeon 34055, Republic of Korea
[25] Snu Astronomy Research Center, Department of Physics & Astronomy, Seoul 08826, Republic of Korea
[26] Department of Astronomy and Space Science, Chungnam National University, Yuseong-gu, Daejeon 34134, Republic of Korea
[27] Instituto de Radioastronomia Millimétrica, E 18012 Granada, Spain
[28] School of Physics and Astronomy, Rochester Institute of Technology, Rochester, NY 14623, USA
[29] National Research Council of Canada, Herzberg Astronomy & Astrophysics Research Centre, Victoria, BC V9E 2E7, Canada
[30] ARC Centre of Excellence for All Sky Astrophysics in 3 Dimensions (ASTRO 3D), Australia
[31] Astrochemistry Laboratory, NASA Goddard Space Flight Center, Greenbelt, MD 20771, USA
[32] Department of Physics & Astronomy, University of South Carolina, Columbia, SC 29208, USA
[33] Leiden Observatory, Leiden University, P.O. Box 9513, 2300 RA Leiden, The Netherlands
[34] Department of Physics and Astronomy, Minnesota State University-Mankato, Mankato, MN 56001, USA
[35] Centre for Extragalactic Astronomy, Department of Physics, Durham University, Durham DH1 3LE, UK
[36] Association of Universities for Research in Astronomy (AURA) for the European Space Agency (ESA), STScI, Baltimore, MD 21218, USA
[37] Center for Astrophysical Sciences, Department of Physics and Astronomy, The Johns Hopkins University, Baltimore, MD 21218, USA
[38] INAF-Osservatorio Astronomico di Trieste, Via Bazzoni 2, 34124 Trieste, Italy
[39] Department of Physics and Astronomy, University of Missouri, Columbia, MO 65211, USA

Abstract

The James Webb Space Telescope (JWST) North Ecliptic Pole (NEP) Time-domain Field (TDF) is a $>14'$ diameter field optimized for multiwavelength time-domain science with JWST. It has been observed across the electromagnetic spectrum both from the ground and from space, including with the Hubble Space Telescope (HST). As part of HST observations over three cycles (the "TREASUREHUNT" program), deep images were obtained with the Wide Field Camera on the Advanced Camera for Surveys in F435W and F606W that cover almost the entire JWST NEP TDF. Many of the individual pointings of these programs partially overlap, allowing an initial assessment of the potential of this field for time-domain science with HST and JWST. The cumulative area of

overlapping pointings is $\sim$88 arcmin^2, with time intervals between individual epochs that range between 1 day and 4 + yr. To a depth of $m_{AB} \simeq 29.5$ mag (F606W), we present the discovery of 12 transients and 190 variable candidates. For the variable candidates, we demonstrate that Gaussian statistics are applicable and estimate that $\sim$80 are false positives. The majority of the transients will be supernovae, although at least two are likely quasars. Most variable candidates are active galactic nuclei (AGNs), where we find 0.42% of the general $z \lesssim 6$ field galaxy population to vary at the $\sim 3\sigma$ level. Based on a 5 yr time frame, this translates into a random supernova areal density of up to $\sim$0.07 transients arcmin^{-2} ($\sim$245 deg^{-2}) per epoch and a variable AGN areal density of $\sim$1.25 variables arcmin^{-2} ($\sim$4500 deg^{-2}) to these depths.

Unified Astronomy Thesaurus concepts: Time domain astronomy (2109); Transient sources (1851); Supernovae (1668); AGN host galaxies (2017); HST photometry (756)

Supporting material: machine-readable table

1. Introduction

With the successful launch, commissioning, and first year of science observations, the James Webb Space Telescope (JWST) has opened new opportunities for the study of the faint (potentially $m_{AB} \gtrsim 30$ mag) variable Universe. After discovering time-varying phenomena (i.e., transients and objects that vary in brightness or position), one would need the capacity to monitor these objects at their astrophysically relevant timescales, to determine the nature of their variability. For example, rapid follow-up of supernovae (SNe) is crucial to determine their types and distances. Flexible follow-up of active galactic nuclei (AGNs) allows the timescale of AGN variability (which can range from several days to several years) to be measured, which can be linked to properties of the supermassive black hole (SMBH) at the center of its host galaxy (e.g., Vanden Berk et al. 2004). However, transient follow-up and variability monitoring with JWST become difficult when Sun angle restrictions, power generation, and micrometeoroid mitigation limit when any particular area of the sky can be observed. The continuous viewing zones (CVZs) centered on the ecliptic poles are the only locations where JWST can observe at any time of the year and avoid these constraints.

Jansen & Windhorst (2018) selected a particularly suitable area within JWST's northern CVZ, the JWST North Ecliptic Pole (NEP) Time-domain Field (TDF), to enable the exploration of time-varying phenomena with JWST at high redshifts, but also within the halo of our own Galaxy and in the extreme outer solar system at high ecliptic latitudes. The JWST NEP TDF is a $>14'$-diameter field centered on (R.A., decl.)$_{J2000}$ = (17:22:47.896, +65:49:21.54) that was carefully chosen to minimize foregrounds, to be devoid of stars brighter than $m_K \sim 15.5$ mag, and to maximize the observing efficiency for time-domain science with JWST. Its location near the NEP allows for follow-up of transients and variable sources at any cadence and at any time of the year. In addition, the NEP suffers minimal zodiacal foregrounds, with minimal variation in the course of a year, naturally allowing for more sensitive observations per unit time. While the ecliptic latitude of the JWST NEP TDF is very high ($b_{ecl} \simeq 86°.2$), it is located at intermediate Galactic latitude ($b^{II} \simeq 33°.6$), providing a clear but relatively long sight line through the halo of our Galaxy. This makes the field useful for deep Galactic time-domain science with JWST as well.

This field serves as an important test bed for advancing our understanding of the time-varying Universe at fainter limits than can be reached from the ground at optical and near-IR wavelengths, where transients and variability can hold cosmological significance (e.g., dark energy, cosmic star formation rate, and the evolution of SMBHs). Type Ia SNe are often used as standard candles to provide critical constraints on the Hubble constant, the mass density of the Universe, the cosmological constant, the deceleration parameter, and the age of the Universe (e.g., Riess et al. 1998). Core-collapse (CC) SNe are equally important, as they not only provide most of the heavy elements in our Universe (e.g., Matteucci & Greggio 1986) but also should trace the rate of instantaneous massive star formation. CC SN rates and their connection to cosmic star formation rates remain poorly understood, as there seems to be a significant mismatch between observed CC SN rates and what is expected (see, e.g., Cappellaro 2014).

In addition to studying transient events like SNe, we can uncover new insights into the nature of astrophysical processes that lead to AGN variability. AGNs are powered by matter accreting onto an SMBH (Lynden-Bell 1969). All massive galaxies host central SMBHs (e.g., Magorrian et al. 1998; Kormendy & Ho 2013), and irregular or varying rates of infall, as well as turbulence and temperature fluctuations, can cause variations in brightness over time. The study of these variable AGNs can provide a better understanding of the complex, unstable processes occurring around SMBHs (e.g., Shakura & Sunyaev 1976; Ulrich et al. 1997; Kawaguchi & Mineshige 1999). As AGNs are linked to the evolution of their host galaxy (e.g., Ferrarese & Merritt 2000; Gebhardt et al. 2000; Kormendy & Ho 2013), this would also allow a better understanding of the coevolution of galaxies and their central black holes.

AGNs are often identified via X-ray or mid-IR emission, colors, or spectroscopic signatures; however, these methods can miss AGNs that are intrinsically faint or lack X-ray emission. Variability in particular provides a unique way to identify AGNs that might be missed via these other methods (e.g., Boutsia et al. 2009; Pouliasis et al. 2019). Lyu et al. (2022) explore various AGN selection methods in GOODS-S, including those based on X-ray emission, UV to mid-IR spectral energy distributions (SEDs), mid-IR colors, radio emission, and variability, and find $\sim$10% of the AGNs in this field to exhibit optical variability.[40] We refer to Lyu et al. (2022, 2023) for a broader treatment of the role of various AGN selection methods.

Variability proves especially promising for identifying faint AGNs, as there appears to exist an anticorrelation between AGN brightness and variability amplitude (Hook et al. 1994; Trevese et al. 1994; Cristiani et al. 1997; Giveon et al. 1999; Vanden Berk et al. 2004; Wilhite et al. 2008; Zuo et al. 2012). In addition, the amplitude or timescale of AGN variability is

---

[40] The optical variable sample is selected from Pouliasis et al. (2019) (10 yr baselines, and five epochs per object).

correlated with accretion disk size and therefore black hole mass (e.g., Xie et al. 2005; Wold et al. 2007; Li & Cao 2008; Wilhite et al. 2008; Burke et al. 2021) and redshift (Cristiani et al. 1990; Hook et al. 1994; Trevese et al. 1994; Vanden Berk et al. 2004). A variability survey can thus provide a more complete census of the AGN population and its evolution over cosmic time. In addition, AGNs identified through variability may be spectroscopically confirmed at any later time.

A large number of studies focusing on AGN variability have been published in the past few years (for a recent review, see Lyu & Rieke 2022). At optical wavelengths, AGNs have been identified via their variability on scales from weeks to years (Sarajedini et al. 2003, 2011; Cohen et al. 2006; Morokuma et al. 2008; Villforth et al. 2010).

As part of Hubble Space Telescope (HST) programs GO 15278 (PI: R. Jansen) and GO 16252/16793 (TREASUR-EHUNT; PIs: R. Jansen and N. Grogin), UV–visible imaging of the JWST NEP TDF was secured with the F275W (0.272 μm), F435W (0.433 μm), and F606W (0.592 μm) filters. Areas of partial overlap between individual visits of the observations allow a first look at two-to-four-epoch object variability and transients in this field. For a detailed description of the observational design of these HST surveys, data reduction, stacked images, and source photometry, we refer the reader to R. Jansen et al. (2024a, 2024b, in preparation).

While previous HST variability studies like Sarajedini et al. (2003; Hubble Deep Field North) and Cohen et al. (2006; Hubble Ultra Deep Field) achieved impressive depths (29.0 and 30.5 mag, respectively), they are limited to approximately ∼6.5 arcmin^2. Villforth et al. (2010), on the other hand, leveraged the expansive area ($\gtrsim$500 arcmin^2) of the Great Observatories Origins Deep Survey (GOODS), but to a relatively shallow depth (∼26.0 mag). At the same exquisite angular resolution (FWHM $\lesssim$ 0″09), TREASUREHUNT observations provide a unique combination of depth ($m_{AB} \lesssim$ 29.5 mag) and area (∼88 arcmin^2) for a variability analysis.

In this work, we provide the first time-domain study of the JWST NEP TDF at visible wavelengths, presenting 12 transients (SN candidates) and ∼100 variable candidates (AGN candidates) identified using TREASUREHUNT data. In Section 2, we briefly summarize the TREASUREHUNT HST data and data processing specific to the detection of transients and variable objects. Section 3 explains our methods for identifying transients and variability in the NEP TDF. In Sections 4.1 and 4.2 we showcase our SN candidate detections and our variable AGN candidates, respectively. All magnitudes are in AB units[41] (Oke & Gunn 1983). Where relevant, we adopt a flat ΛCDM cosmology with $H_0 = 68$ km s^{-1} Mpc^{-1}, $\Omega_m = 0.32$, and $\Omega_\Lambda = 0.68$ (Planck Collaboration et al. 2016, 2020).

2. Data and Processing

2.1. HST Observations and Data Processing

Observations from HST GO 15278 were taken between 2017 October 1 and 2019 February 9, and those from GO 16252 +16793 (TREASUREHUNT[42]) were taken between 2020 September 25 and 2022 October 31. The former program targeted the central ($r \lesssim 5'$) portion of the JWST NEP TDF, and the latter targeted an outer annulus to $r \sim 7\farcm8$. Together, these programs provide near-contiguous coverage with the Wide Field Camera 3 (WFC3/UVIS) in the F275W filter ($\lambda_c \sim$ 0.272 μm) and with the Advanced Camera for Surveys (ACS/WFC) in the F435W and F606W filters ($\lambda_c \sim$ 0.433 and ∼0.592 μm), with a total area of ∼194 arcmin^2 (ACS/WFC). The full HST coverage of the JWST NEP TDF is shown in Figure 1.

As described in more detail in R. Jansen et al. (2024a, 2024b, in preparation), both programs used four-orbit CVZ and pseudo-CVZ[43] visits to reach 2σ limiting depths of $m_{AB} \simeq 28.0$, 28.6, and 29.5 mag in F275W, F435W, and F606W, respectively. These limiting depths were determined using the SExtractor (Bertin & Arnouts 1996) MAG_AUTO aperture, within areas with single-epoch coverage (lighter gray in Figure 1), and are the adopted nominal survey depths.

The TREASUREHUNT data were retrieved from MAST and postprocessed (after the standard ACS and WFC3 calibration pipeline steps of flat-fielding and correction for charge transfer efficiency (CTE) effects) to mask satellite trails, remove residual CTE trails, and fit and subtract the background (R. Jansen et al. 2024a, 2024b, in preparation). The last was needed because the observing strategy deliberately used the full duration of CVZ orbits, as well as pseudo-CVZ orbits where HST was allowed to dip closer to the Earth limb than the nominal limit for CVZ orbits. This resulted in excess background light that helped fill charge traps in the F275W exposures with their exceedingly dark natural sky background (e.g., O'Brien et al. 2023), but it also rendered the observed background level meaningless.

The background-subtracted images were corrected for geometric distortion and aligned to the Gaia/DR3 (Gaia Collaboration et al. 2016, 2023) astrometric reference grid using the DrizzlePac tasks TweakReg and Astro-Drizzle (see Hoffmann et al. 2021). The AstroDrizzle software also flags cosmic rays (CRs), a crucial step when identifying faint variability, where CR-induced signals could cause spurious variability if not properly removed. We expect, and tested (as discussed in more detail in the Appendix), that all CR and other image artifacts were largely removed through the AstroDrizzle step, as each single four-orbit visit resulted in eight to nine exposures per filter that were stacked together.

All eight to nine exposures per visit were taken at the same pointing with small $\leqslant 0\farcs2$ dither offsets in R.A. and decl. For each visit, we drizzle-combined the individual postprocessed, rectified, and aligned exposures per filter (R. Jansen et al. 2024a, 2024b, in preparation). For ACS/WFC F606W and F435W, this resulted in 24 rectified and aligned science images (and 24 associated weight maps), and for WFC3/UVIS F275W this resulted in 23 images and associated weight maps, each at a pixel scale of 0″030 pixel^{-1} and centered on the nominal field center of the JWST NEP TDF. We also use the full mosaics of all drizzle-combined images per filter, generated with the same image dimensions and pixel scale and aligned to Gaia/DR3 to within 0″008 in R.A. and decl.

The footprints of individual ACS/WFC (and to a lesser extent WFC3/UVIS) visits partially overlap one another, with

---

[41] Defined as $m_{AB} = -2.5 \log(F_\nu) + 8.90$ mag, where the flux density F_ν is in Jy.
[42] We will loosely refer to the observations and data of the GO 15278 program as also part of TREASUREHUNT hereafter, as the intent and survey strategy were identical.

[43] True CVZ orbits imply Earth limb angles $\gtrsim$15°5, but uninterrupted observations can be implemented at smaller angles down to ∼7°6 away from the Earth limb when phased to execute when that limb is dark. We term these possible but nonstandard opportunities "pseudo-CVZ."
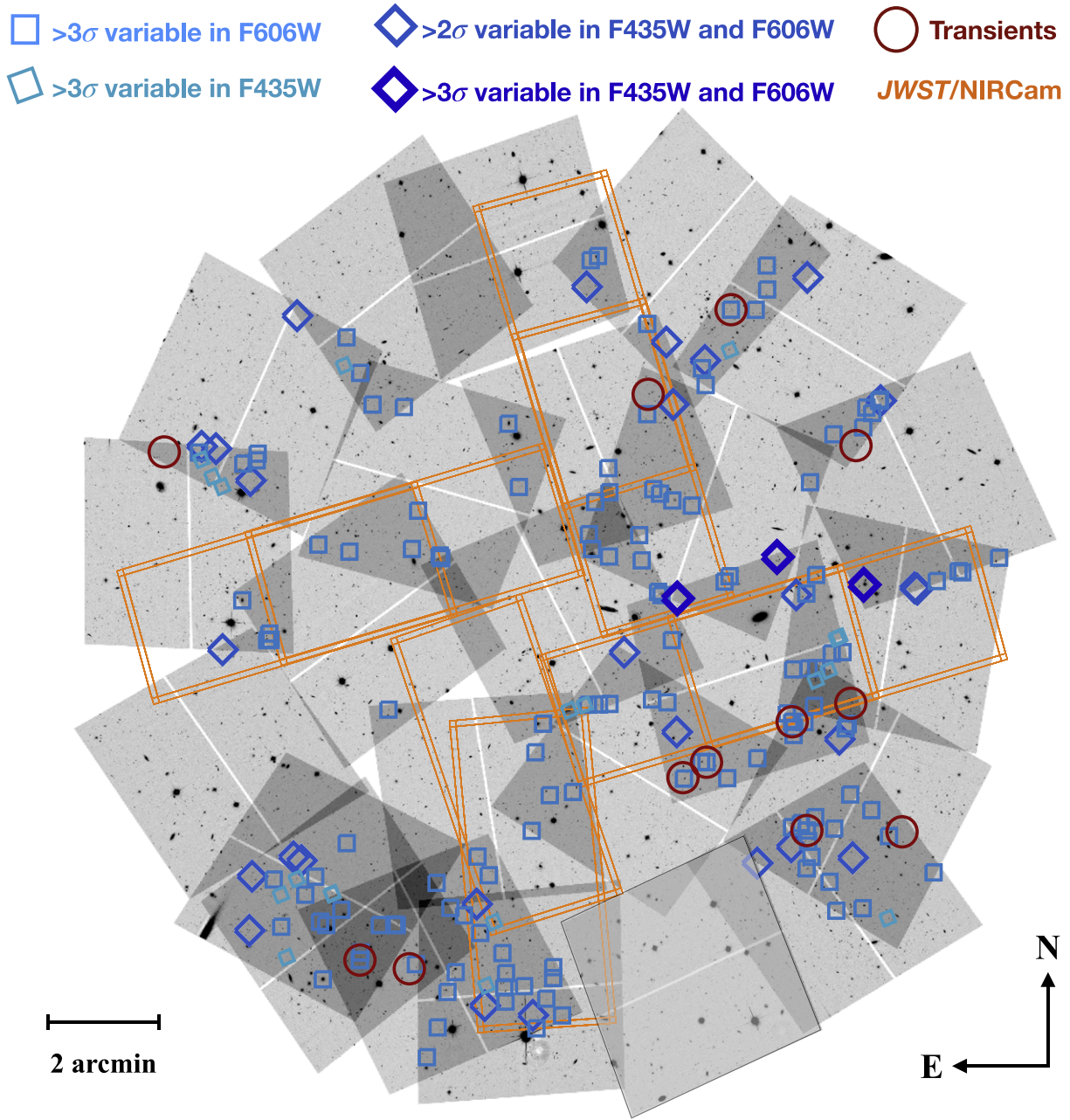
Figure 1. Full extent of HST ACS/WFC coverage of the JWST NEP TDF. Regions of overlap between visits in the mosaic are highlighted in progressively darker shades of gray for areas of two-, three-, and four-epoch overlap. This paper focuses on these regions of overlap, with a total area of 87.94 arcmin^2, to investigate transients and variable sources. Red circles mark the positions of the 12 identified transients, while blue squares and diamonds mark the 190 unique variable candidates discovered in this study. We expect ∼80 of these sources to be false positives (see Section 3.2). Symbol shapes and colors identify the samples from which individual variables were selected, as indicated by the legend at the top of the figure. For comparison, the JWST/NIRCam coverage of this field is outlined in orange. We estimate photometric redshifts (Section 4.3) for objects with both HST and JWST photometry. One visit (jeex02; at lower right) with a bad astrometric solution was ignored in this work.

a cumulative area of overlap of ∼88 arcmin^2. These overlapping regions are key to searching for transients and variability within this field. Figure 1 showcases the overlapping regions in progressively darker shades of gray for areas of two-, three- and four-epoch overlap. The time interval between observations in these regions of overlap ranges between 1 day and 4+ yr.

We note that while the very small number of epochs and sparse time sampling can catch transients like SNe and variable sources like AGNs, they cannot provide a light curve to trace their evolution. Further epochs would provide a more robust identification of variable sources, where we may characterize

the scatter in the measured brightness (e.g., Sokolovsky et al. 2017; Pouliasis et al. 2019).

While our primary focus is the identification of time-variable objects within the TREASUREHUNT HST data, we opt to incorporate ancillary data to better understand certain objects of interest. Specifically, we incorporate JWST/NIRCam (0.8–5 μm), NuSTAR, XMM-Newton, Chandra, and MMT/Binospec data.

2.2. JWST Observations and Data Processing

JWST/NIRCam observations within the JWST NEP TDF were obtained between 2022 August 25 and 2023 May 30 as

part of JWST GTO 2738 (PIs: R. Windhorst and H. Hammel) in seven broadband filters (F090W through F444W) and one medium-band filter (F410M) as part of the PEARLS program (Windhorst et al. 2023). Figure 1 shows the JWST observations outlined in orange, highlighting the four epochs, corresponding to the four orthogonal "spokes." Each spoke consists of two NIRCam pointings that partially overlap in the center. Each pointing includes a total exposure time of 3.5 hr across all eight filters, or about 3000 s per filter. Each spoke has an area of 13′.7, totaling 54′.7 of JWST observations.

The data were retrieved from MAST and postprocessed by the PEARLS team using their custom pipeline to mitigate $1/f$ noise, alleviate wisps in the NIRCam/SW filters, mask snowball artifacts, and flatten the background across readout amplifier boundaries. The individual postprocessed images where rectified and aligned to Gaia/DR3 independent of the HST images, but using nearly identical methods. Full mosaics of the field were created for each filter with a 0″.03 plate scale. The 5σ point-source limit is typically between 28.0 and 29.1 mag, depending on the filter. For more details on the reduction, calibration, and postprocessing, we refer to Windhorst et al. (2023), Robotham et al. (2023), and R. Jansen et al. (2024c, in preparation). In Section 4.3, we will use PEARLS aperture photometry of transient and varying objects discovered in areas with both HST and JWST coverage to fit SEDs.

2.3. X-Ray Observations and Data Processing

The JWST NEP TDF has also been observed extensively in X-rays with NuSTAR, XMM-Newton, and Chandra. NuSTAR has monitored the field since Cycle 5 (PID 5192, 6218, 8180, and 9267; PI: F. Civano). For this work we use the Cycle 5+6 data and catalog published in Zhao et al. (2021a, 2021b, 2024). The 21 NuSTAR observations took place over 28 months (between 2019 September and 2022 January), while the three XMM-Newton observations (part of the NuSTAR Cycle 6 program) were taken over 15 months (between 2020 October and 2022 January). The total NuSTAR exposure from Cycle 5 +6 is 1.5 Ms, reaching a flux limit of 3.3×10^{-14} erg cm^{-2} s^{-1} in the 3–24 keV band. We note that this is the deepest NuSTAR field taken thus far. The total XMM-Newton exposure time is 62 ks, reaching a limit of 8.7×10^{-16} erg cm^{-2} s^{-1} in the 0.5–2 keV band.

We also use the first 1.3 Ms of Chandra observations of the JWST NEP TDF (PID 19900666, 20900658, 21900294, and 22900038; PI: W.P. Maksym) spanning Cycles 19–23. Chandra observed the field 46 times between 2018 April 12 and 2022 September 25 (a span of 4.6 yr), with exposures ranging from 9 to 59.9 ks. Beginning on 2021 August 29, these occurred in 90 ks epochs every 3 months, typically broken into two or more individual visits (ObsIDs) spanning no more than 30 days per epoch. We reprocessed and reduced the data using `ciao` (Fruscione et al. 2006), corrected the cross-observations using source catalogs generated by `wavdetect`, and astrometrically registered them to Pan-STARRS (Chambers et al. 2016). We then used `merge_obs` to generate combined event files and exposure maps. The faintest 3σ detection in the catalog is 1.35×10^{-16} erg s^{-1} cm^{-2} in the full 0.5–7 keV band assuming galactic absorption and a $\Gamma = 1.4$ power law.

2.4. Ground-based Spectroscopy

MMT/Binospec (Fabricant et al. 2019) observations of the JWST NEP TDF in 2019 September (PI: C. Willmer) used a 270 line mm^{-1} grating and a 1″ slit width to yield spectra spanning ~3900–9240 Å sampled at 1.30 Å pixel^{-1} and with a resolution of ~4.9 Å (FWHM) at 6500 Å. The exposure time was 1 hr (4×900 s), reaching signal-to-noise ratio ~ 5 at m_{AB} ~ 22.5 mag for quiescent galaxies and a magnitude deeper for galaxies with significant emission lines.

3. Methods to Identify Transients and Variability

In this section, we detail our methods for identifying transients and variability in the 55 areas of overlap (shown as darker shades of gray in Figure 1) with a combined area of ~88 arcmin^2.

Transients are usually defined as objects that only appear for a short duration. For this work, where we expect most transients to be SNe, we consider relatively bright point sources that are present in one epoch yet do not appear in another. We searched for transients using difference images and considered any source detected therein a transient candidate. In contrast, variable sources tend to show less extreme differences in brightness and are not as evident in difference images. Variable sources are therefore identified after measuring the source flux and its associated uncertainty within a small aperture. Consequently, some sources we identify as transients may be variable sources with extreme amplitudes of variability (e.g., quasars), and some variable sources may be dim transients or transients caught well away from peak brightness (e.g., SNe). Nonetheless, we assume that most transients we discover will be SNe, while most variable sources will be weak AGNs. However, the methods presented here may identify a variety of objects, including variable stars, tidal disruption events, gamma-ray bursts, and quasars. We did not identify any objects that showed appreciable movement between visits. For all objects discovered here, further analysis is required to determine their true nature.

3.1. Transient Search

Transients were identified by visual inspection of difference images, each of which was created as follows. First, we bring the drizzled images of individual visits to the same pixel grid using their Gaia-aligned world coordinate system (WCS) and the Astropy (Astropy Collaboration et al. 2013, 2018, 2022) affiliated package `reproject`. Then, we generate two distinct difference images for each overlapping region in the deeper F606W images, i.e., 110 difference images for the 55 overlapping areas. For instance, if Visit 1 overlaps with Visit 2, we generate one difference image by subtracting Visit 2 from Visit 1 and another difference image by subtracting Visit 1 from Visit 2. In each difference image we then visually identify sources with positive flux that are consistent in appearance with bearing the imprint of the point-spread function (PSF). We did not use the F435W images for our transient search because they are ~0.9 mag shallower.

Although rare, bright CR-induced signals can sometimes survive in final drizzled products and subsequently appear in difference images. We inspected the individual pipeline-calibrated, flat-fielded exposures at the corresponding position of each transient candidate to ensure that they appear in each exposure, bear the imprint of the PSF, and are not (residuals of)

Table 1
Relevant SExtractor Parameters for Variability Identification and Aperture Photometry

Parameter	Variability Aperture	Full Aperture
Aperture size	0″24	FLUX_AUTO
DETECT_MINAREA	5	5
DETECT_THRESH	1.5	1.5
ANALYSIS_THRESH	1.5	1.5
DEBLEND_MINCONT	0.001	0.06
FILTER_NAME	gauss_3.0	gauss_3.0
GAIN	*median exposure time*	
BACK_SIZE	128	128
BACK_FILTERSIZE	3	3
BACKPHOTO_THICK	50	50

Note. For each SExtractor parameter in the first column, the second and third columns list its value for identifying variable sources and for full aperture photometry, respectively. We used a circular aperture with a diameter of 0″24 for variability identification, specified using the PHOT_APERTURES parameter, and the FLUX_AUTO aperture for full aperture photometry. We set the GAIN value to the median exposure time of the individual exposures combined per visit.

CRs or other spurious noise. We originally found 20 transient candidates, of which 8 were confirmed to be due to CRs and were removed from further consideration.

We measured the apparent F606W magnitudes of each transient using the difference images. To measure transient magnitudes, we centered a circular aperture with a radius of 8 pixels on the transient in the difference image and measured its magnitude within that aperture. These apertures are $\gtrsim 5\times$ the FWHM of the PSF and encompass the transient signal. We used the Python photometry package Photutils (Bradley et al. 2022) and specified the exact center of each aperture. We created a difference error map by adding the weight (WHT) maps from the individual visits in quadrature and then taking $\mathrm{ERR} = 1/\sqrt{\mathrm{WHT}}$. We direct this error map into Photutils to derive an uncertainty on the reported flux. Magnitude errors are then calculated as $\Delta m = (2.5/\ln 10) \cdot \sigma_F/F$, with F the measured flux and σ_F the uncertainty thereon, both as reported by Photutils.

For each transient, we also performed matched-aperture photometry on a subset of F435W difference images, generated for those regions of overlap that contained a transient.

3.2. Variability Search

To detect variability in galaxies, we first constructed source catalogs using SExtractor, with object positions and aperture photometry for each visit. For initial object detection, as summarized in Table 1, we require an object to be detected at the 1.5σ level above the local sky level (given a gain value corresponding to the median exposure time of the individual exposures in that visit and filter) after smoothing with a Gaussian kernel with an FWHM of 3 pixels, and we require a minimum number of 5 contiguous pixels to minimize detection of spurious sources. For the same reason, we also generously masked the pixels along the detector borders, where fewer contributing exposures result in excess noise and imperfect rejection of CR signal.

We compared brightness measurements across distinct visits to identify potential variables. We specifically focus on detecting variability in the F435W and F606W filter
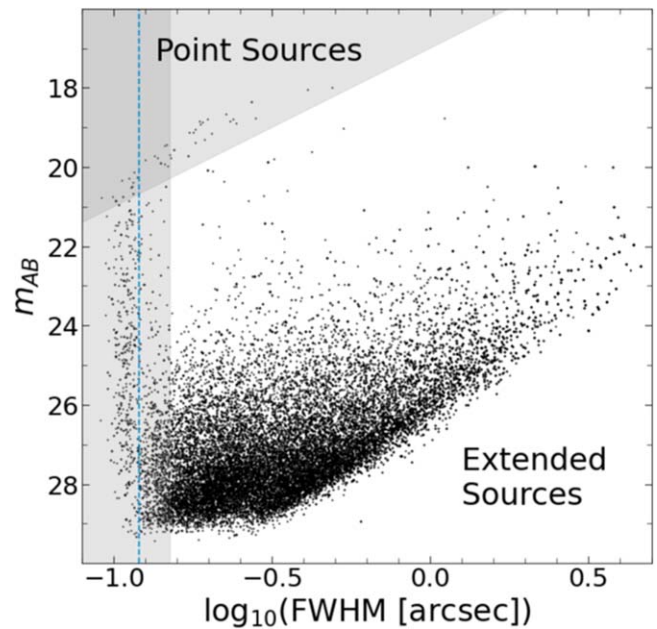

Figure 2. Star–galaxy separation, following Windhorst et al. (2011), using the SExtractor MAG_AUTO magnitudes in F606W vs. FWHM. Objects within gray regions, with FWHM < 0″15 or $m_{AB} < 17 - 4\log_{10}(\mathrm{FWHM})$ mag, are flagged as stars and are not considered in this study. We also show the radius (0″12) of the aperture used to identify variability as a vertical blue dashed line.

observations, as the F275W filter magnitude limit is substantially brighter, the total area of overlap between individual F275W visits is substantially smaller, and the WFC3 F275W observations are not contemporaneous with the ACS/WFC F435W and F606W ones.

3.2.1. Photometry

Our goal is to leverage HST's high resolution to isolate the potentially varying nuclei within galaxies and SNe near their core while ignoring the nonvarying extended component. To achieve this, we first set the minimum contrast for deblending in SExtractor (DEBLEND_MINCONT) to 0.001. This value is lower than is typical but allows for isolating the nuclei of galaxies *and* potentially locating variability in bright regions that may not be in the very center of a galaxy. In addition to a low deblending threshold, we opted to use apertures close to the FWHM of stellar objects. For our resolution of $\lesssim 0″09$, we used a circular aperture with a diameter of 0″24 (8 pixels). For apertures much larger than this, the surrounding galaxy tends to dilute any variability of a compact central source. We henceforth refer to this small aperture as the 0″24 aperture and to the corresponding magnitudes as $m_{0.24}$. The radius of this aperture is shown as the dashed blue vertical line in Figure 2 to facilitate comparison with detected stellar objects.

With DEBLEND_MINCONT = 0.001, the measured variability sometimes appears offset from the centers of galaxies. This could be due to off-center SNe or SMBHs that have yet to settle onto the centers of their host galaxies. To measure host galaxy properties for these offset events, we also ran SExtractor with DEBLEND_MINCONT = 0.06, which reduces deblending of galaxies into individual clumps. We thus have two types of aperture photometry for each source: (1) within the small circular 0″24-diameter aperture used to identify variability, and (2) for the full Kron aperture, as identified by SExtractor. Table 1 summarizes the relevant

SExtractor parameters used for these two types of measurements. For our matched-aperture F435W photometry, we used SExtractor in dual-image mode, employing the full F606W mosaic as the detection image.

To identify variability, we need to first carefully match the objects from one visit catalog to another. We did so using the Astropy match_coordinates_sky function, which finds the nearest object in the catalog from one visit to a given object in a catalog from another. To ensure that slight differences in position do not contribute to the measured variability, we only considered two sources to be a match across two different visits if they are within 1 pixel of each other ($0\rlap{.}''03$). We increased this threshold to $0\rlap{.}''08$ when matching the F606W catalog to the F435W catalog, to account for the fact that objects may have different PSF and surface brightness distributions at different wavelengths. Matches between the DEBLEND_MINCONT = 0.001 and DEBLEND_MINCONT = 0.06 catalogs were identified using a search radius of $3''$, since the highly deblended catalog may find variability in the outskirts of host galaxies, and thus the positions may be offset by much more than our astrometric uncertainties and pixel size.

We opted to ignore stars in our variability analysis owing to uncertainties in the ACS PSF (e.g., Villforth et al. 2010). We flagged as stars all objects with an FWHM less than $0\rlap{.}''15$ or $m_{AB} < 17 - 4\log_{10}(FWHM)$ mag. Gray shading in Figure 2 indicates the stars and faint pointlike sources that were removed from our analysis. In addition, we ignored objects with a SExtractor FLAGS[44] > 2, including objects with saturated pixels, truncated footprints, corrupted apertures/ footprints, or other issues. Lastly, we also ignored all objects within the jeex02 visit in the F606W filter, as it has a poor astrometric solution that hampers reliable alignment and variability measurements (R. Jansen et al. 2024a, 2024b, in preparation).

Some variable candidates, like variable stars and ultrabright AGN-like quasars, will be pointlike and excluded by our methods. Missing quasars in particular may bias our final AGN estimates. Nonetheless, these objects are relatively rare. In addition, our methods would miss any AGN that does not vary on the timescales we probe. Variability identified in this paper is therefore the *minimum* amount of variability expected in this field.

3.2.2. Variable Source Selection

Sources were identified as variable if they varied by more than $3\times$ their combined photometric uncertainty. Therefore, careful consideration of uncertainties is crucial to ensure that variable sources are robustly identified. Combining and resampling multiple lower-resolution images into a higher-resolution composite image (using, e.g., the drizzle algorithm) causes both the signal and the noise in adjacent pixels to become correlated. Photometric uncertainties are known to be underestimated when correlated pixel noise is not taken into account (e.g., Casertano et al. 2000; Labbé et al. 2003; Blanc et al. 2008; Whitaker et al. 2011; Papovich et al. 2016). In addition, the ACS PSF is known to vary owing to telescope breathing (e.g., Villforth et al. 2010), which could potentially contaminate variability identification performed within small apertures. Finally, CRs may cause changes in brightness if not filtered out properly. We employed an empirical approach to

---

statistically account for correlated pixel noise and PSF changes, as well as other sources of error, regardless of their origin.

Figure 3 highlights our method to best calibrate photometric uncertainties, which is based on the variability search methods of Cohen et al. (2006). Measured magnitudes were compared for all objects that appear in more than one visit. For each such object, Figure 3 shows the magnitude difference, $\Delta m_{0.24}$, versus the mean magnitude, $m_{0.24}$. We used the distribution of these magnitude differences to calibrate the empirical (true) photometric scatter, where the inner brown curves contain $\sim$68.26% of the data points in each magnitude bin (shown as black circles and curves). To account for correlated pixel noise, a varying PSF, and other unaccounted-for sources of error, we multiplied all SExtractor magnitude errors by a fixed scale factor (1.15 for F606W and 1.35 for F435W) to best match the observed distribution of photometric scatter. The scaled result is represented by the large brown circles. Magnitude difference uncertainties (for F606W) were calculated as

$$\sigma_{\Delta m} = 1.15 \times (2.5\, N / \ln 10)\sqrt{(\sigma_1/F_1)^2 + (\sigma_2/F_2)^2}, \quad (1)$$

with N the number of sigma, F_1 (F_2) the measured flux for Visit 1 (Visit 2), and σ_1 (σ_2) the corresponding scaled flux error.

We emphasize that Figure 3 is used to calibrate photometric uncertainties and *not* to identify variable candidates. The blue squares represent objects flagged as variable at $\geqslant 3\sigma_{\Delta m}$ in F606W. These objects are determined to be those that vary by more than $3\times$ their individual photometric uncertainty. In general, these sources fall outside the brown 3σ curves in Figure 3, but this is not always the case. Some objects outside the brown 3σ curves are not flagged as variable if their individual photometric uncertainties are larger than the median. Similarly, some objects inside the brown 3σ curves are flagged as variable if their individual photometric uncertainties are smaller than the median.

In general, we do not expect zero-point offsets between visits to be a concern, as changes in zero-point over the duration of the TREASUREHUNT program are <1% for ACS/WFC (Bohlin et al. 2020; O'Brien et al. 2023). The histogram on the right side of Figure 3 is centered at $\Delta m_{0.24} = 0.02$ mag (with a standard deviation of 0.25 mag that is dominated by the photometric uncertainties of faint sources), therefore showing that the zero-points between detectors and different regions on the same detector as calibrated by the standard HST pipeline are correct to $\lesssim 0.02$ mag.

We only considered objects brighter than $m_{0.24} \simeq 28.6$ mag in F435W or $m_{0.24} \simeq 29.5$ mag in F606W (corresponding to the predicted 2σ magnitude limits for sources in the field) in at least one epoch. We manually sorted through variable candidates and removed 63 sources that either are contaminated by diffraction spikes from a bright star or are close to the edge of a detector. In a vast majority of these cases a diffraction spike overlapped the object in one visit but not in another, observed at a different orientation.

We created a variability catalog for objects that vary more than $3\sigma_{\Delta m}$ in F435W and, similarly, a variability catalog for objects that vary more than $3\sigma_{\Delta m}$ and $5\sigma_{\Delta m}$ in F606W. In addition, we created catalogs with sources that vary (in the same direction) in *both* filters with $2\sigma_{\Delta m}$ and $3\sigma_{\Delta m}$ significance. The significance of the catalogs for objects that vary in both filters to $2\sigma_{\Delta m}$ is $\sqrt{2}\,(2\sigma_{\Delta m}) \simeq 2.83\sigma_{\Delta m}$, and that to $3\sigma_{\Delta m}$ is $\sqrt{2}\,(3\sigma_{\Delta m}) \simeq 4.24\sigma_{\Delta m}$. We consider the latter sample (variability detected in both filters to $3\sigma_{\Delta m}$) to be our
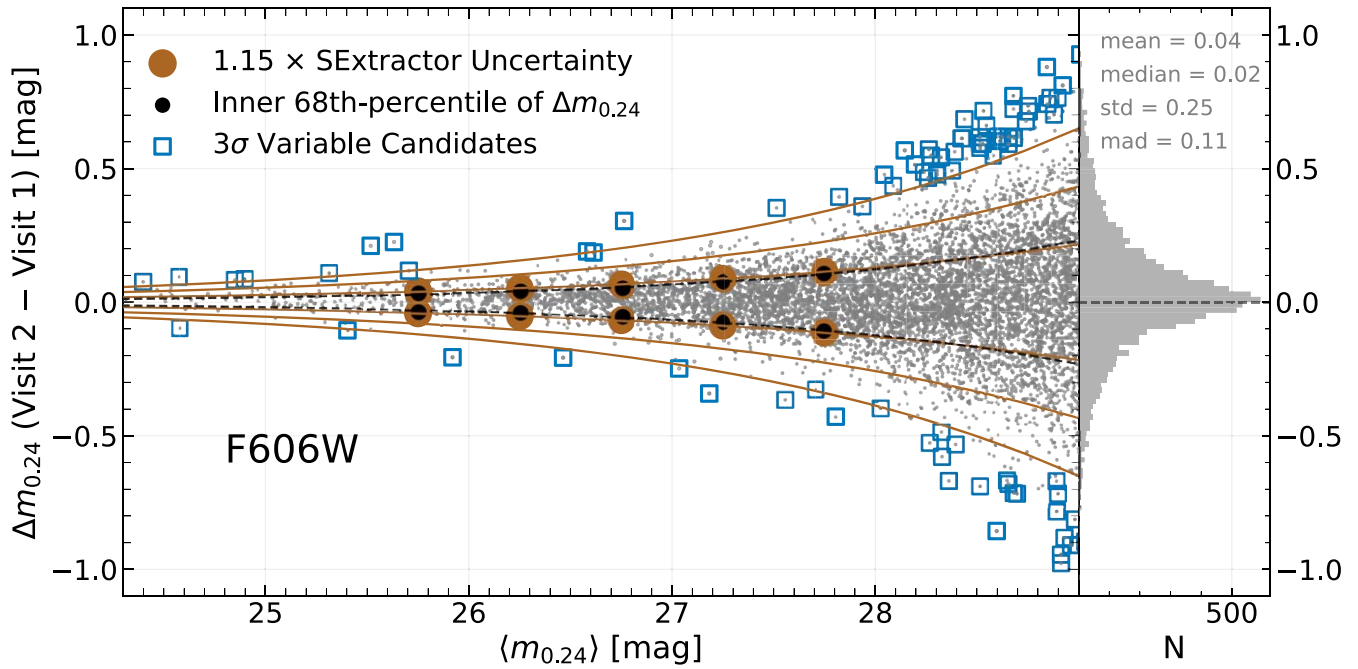

Figure 3. Calibration of photometric uncertainties to identify variable sources. We plot the difference in measured F606W magnitude, $\Delta m_{0.24}$, vs. the average measured F606W magnitude, $m_{0.24}$, for objects observed more than once in regions of overlapping HST coverage, where $\Delta m_{0.24}$ is defined in the sense Visit 2 − Visit 1. Each small gray point is an individual object, as detected and measured with SExtractor. The large brown circles depict SExtractor photometric errors, scaled by a factor 1.15 to match the observed distribution of magnitude differences (shown as small black circles) measured in 0.5 mag wide bins for $25.5 < m_{0.24} \leqslant 28.0$ mag such that ∼68.3% of all data points fall between them. The dashed black curves represent the inner ∼68.3% range of the distribution at each magnitude and are polynomial fits to the black points. The brown curves therefore represent *median* 1σ, 2σ, and 3σ ranges as fit to the brown circles. Blue squares identify objects that vary at $\geqslant 3\sigma_{\Delta m}$ in F606W, where $\sigma_{\Delta m}$ is defined in Equation (1). The histogram on the right-hand side illustrates the distribution of magnitude differences for all objects detected in the field. In gray, we list mean, median, standard deviation, and median absolute deviation of the *y*-axis distribution.

most conservative, robust sample, as objects that vary in both filters are most likely to be true variables, although the shallower F435W images severely limit their number.

3.2.3. Accounting for False Detections

Since variable sources are identified using $2\sigma_{\Delta m}$ or $3\sigma_{\Delta m}$ significance levels, we can expect false detections (e.g., noise peaks). We herein refer to the individual variable sources identified in this work as variable candidates, since we cannot determine which individual sources exhibit genuine variability and which are spurious detections.

We predict the number of false detections using Gaussian statistics. As demonstrated in Figure 4, we observe a Gaussian distribution in $\Delta m_{0.24}$ for all 4059 galaxies with 28.0 mag $< m_{AB} < 28.5$ mag. We confirm that brightness bins of 25.0 mag $< m_{AB} < 27.0$ mag (2550 galaxies), 27.0 mag $< m_{AB} < 28.0$ mag (4892 galaxies), and 28.5 mag $< m_{AB} < 29.0$ mag (5336 galaxies) similarly follow a Gaussian distribution.

Given a Gaussian distribution, we expect a false detection rate of 0.27% (assuming a two-tailed test, where the difference in magnitude can be either positive or negative) for variable candidates identified at $3\sigma_{\Delta m}$ significance. That rate falls rapidly for levels higher than $3\sigma_{\Delta m}$. We also identify variable candidates that vary in *both* filters (in the same direction) with $2\sigma_{\Delta m}$ and $3\sigma_{\Delta m}$ significance. Since we implement the requirement that the variability must be of the same sign in both filters, we estimate the amount of false detections using a one-tailed test (i.e., 0.135% false detections at $3\sigma_{\Delta m}$) for these samples.

To demonstrate the methodology by which we assessed the number of false positives as a function of the significance of the detected variability, Figure 5 shows the number of detected
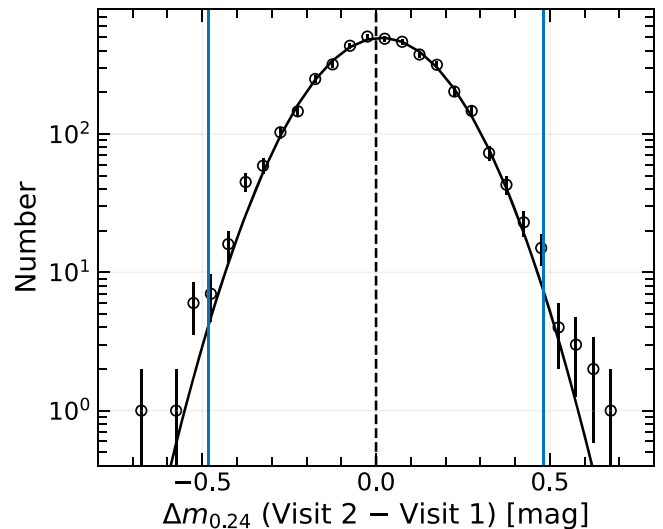

Figure 4. Histogram of the distribution of magnitude differences measured between two epochs ($\Delta m_{0.24}$) for all galaxies (4059 total) between 28.0 mag $< m_{AB} < 28.5$ mag. The black circles show the number of galaxies (*N*) for each $\Delta m_{0.24}$ bin, where the error bar is $\sqrt{N}$. The solid black curve is a Gaussian fit to the data. The vertical blue lines represent the 3σ thresholds based on the Gaussian fit. This proves that the distribution of $\Delta m_{0.24}$ follows a Gaussian distribution, such that the false detections can be assumed to follow Gaussian statistics (see Section 3.2.3).

variable candidates, the expected number of false positives (and percentage of the total number of objects in the parent sample), and the number of genuine variable sources in $0.5\sigma_{\Delta m}$ wide bins for the F606W sample that varies by more than $3\sigma_{\Delta m}$ and the F435W+F606W sample that varies by more than $2\sigma_{\Delta m}$.
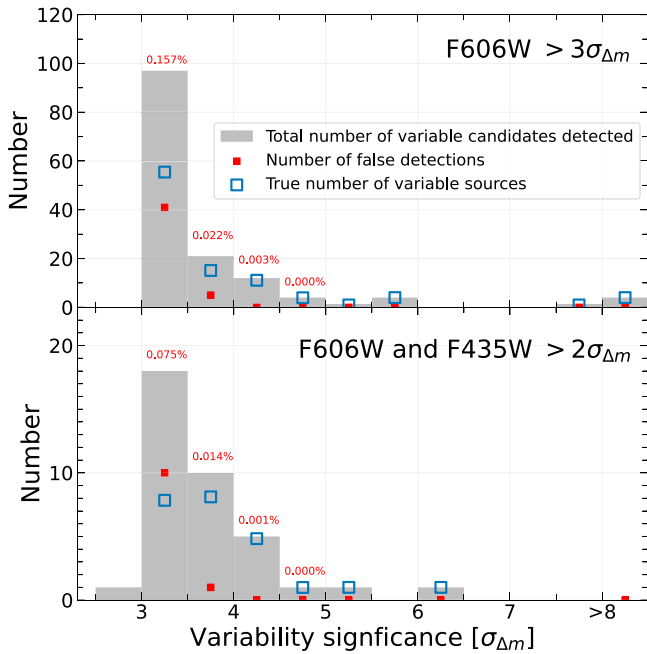
Figure 5. Histograms of the number of variable candidates (light gray) and estimated numbers of false positives (red) and genuine variable sources (blue) as a function of the significance (in units of $\sigma_{\Delta m}$) of the variability detected. The number of genuine variables and the number of false positives add up to the total number of candidates in each bin. The red labels above each bin show the percentage of all objects in the field that are expected to be false positives for that $\sigma_{\Delta m}$ bin. The top panel is for sources that varied by more than $3\sigma_{\Delta m}$ in F606W, and the bottom panel is for sources that varied by more than $2\sigma_{\Delta m}$ in both F606W and F435W, and did so in the same sense. Hence, assuming Gaussian statistics, the top panel reflects a two-sided test, and the bottom panel reflects a one-sided test. In total, we estimate ∼80 false positives in the sample of sources that varied by more than $3\sigma_{\Delta m}$ in F606W, the sample of sources that varied by more than $3\sigma_{\Delta m}$ in F435W, and the sample of sources that varied by more than $2\sigma_{\Delta m}$ in both F606W and F435W.

In addition to false detections due to Gaussian statistics, image artifacts like CRs, hot pixels, bias stripping, amplifier offsets, CTE trails, dust motes, optical ghosts, and cross talk may cause artificial variability to be detected. Of these, CRs are the brightest and most prevalent, yet they will not affect our results as a result of robust flagging and having eight exposures (per pointing, filter and epoch) to stack using the `Astro-Drizzle` software. We explore this in more detail in the Appendix. The other image artifacts are largely removed by the standard HST pipeline. Therefore, we do not expect and find no evidence for image artifacts to bias our results. Nonetheless, confirmation of which individual sources genuinely vary will require follow-up observations.

4. Results

In this section, we present our findings regarding the identification and characterization of transients and variable objects in our data set. We detected a total of 12 transients, including two quasar candidates, and 190 unique galaxies exhibiting variability (where ∼80 are expected to be false positives). Figure 1 provides a visual representation of the locations of both the transient (red circles) and variable candidates (blue squares and diamonds). Variable candidates are identified in almost all areas of overlap, except those with insufficient astrometric precision or excess noise.

We note that the techniques used to identify transients and variable candidates (as described in Section 3) cause some objects detected as variable candidates to also be classified as transient candidates (e.g., the quasars). Rather than appearing and then disappearing, these actually vary in brightness over time with a sufficiently large amplitude that they were detectable in our difference images.

4.1. Transients in the JWST NEP Time-domain Field

We identified a total of 12 transients, for each of which we show $3'' \times 3''$ cutouts of the F606W images from the relevant visits and of the corresponding difference image in Figure 6. For each of these transients, Table 2 lists the coordinates, data set IDs, and date of observation of each visit; the time interval between epochs; and the measured apparent brightness (difference in magnitude between the two epochs) in F606W. We also report the F435W magnitude, if the matched-aperture flux exceeded the F435W detection limit. We call the epoch in which the transient signal appears "Visit 1." The transients range in brightness from $m_{AB} \sim 24.8$ to ∼27.5 mag in F606W. This may not correspond to the peak brightness of the transient, as the measured brightness depends on when the transient event image was taken during its respective light curve. At magnitudes fainter than $m_{AB} \sim 27.5$ mag, the difference images become dominated by image noise, preventing reliable identification of transients.

In all, we detected ∼0.14 transients arcmin^{-2} of overlapping area, or ∼491 deg^{-2}. Since two epochs are needed to detect a transient, the areal density per epoch is therefore ∼0.07 transients arcmin^{-2} (∼245 deg^{-2}), or ∼0.77 per ACS/WFC footprint per epoch. For comparison, Dahlen et al. (2012) searched for SNe in the GOODS fields (using the ACS/F850LP filter) and identified 118 SNe in a total area of 1 deg^2 to $m_{F850LP} \sim 26$ mag. If we only consider the four transients with $m_{F606W} \lesssim 26.0$ mag, we find an areal density of ∼164 deg^{-2}, consistent with Dahlen et al. (2012) when factoring in differences in detection filter, SN colors and redshift distribution, and small number statistics. We also note that it is likely that not all our transients are SNe.

4.1.1. Transients with Significant X-Ray Detections

Next, we checked whether any of the transients were detected in X-rays within XMM-Newton, NuSTAR, or Chandra observations of the field. We matched the transient positions with published and preliminary X-ray source catalogs and found that three of the transients are noticeable X-ray emitters. While an in-depth analysis of the X-ray observations of these sources is beyond the scope of the present paper and is deferred to future work, we present the measured XMM-Newton, NuSTAR, and Chandra fluxes in Table 3.

For the XMM-Newton and NuSTAR catalogs, we used a matching radius of $5''$ and $30''$, respectively, and found a likely match for transients T7, T10, and T11. We inspected the Chandra 0.5–7 keV event-file images for obvious sources, and here we also identified sources consistent with T7 and T10. For the other transients, we extracted source counts from a region with a radius of $2''$ and background counts from a nearby source-free region with a radius of $10''$, but we found no evidence for any X-ray counterparts above 1σ significance. Chandra upper limits vary across the field owing to detector geometry, as well as vignetting and PSF spreading for off-axis
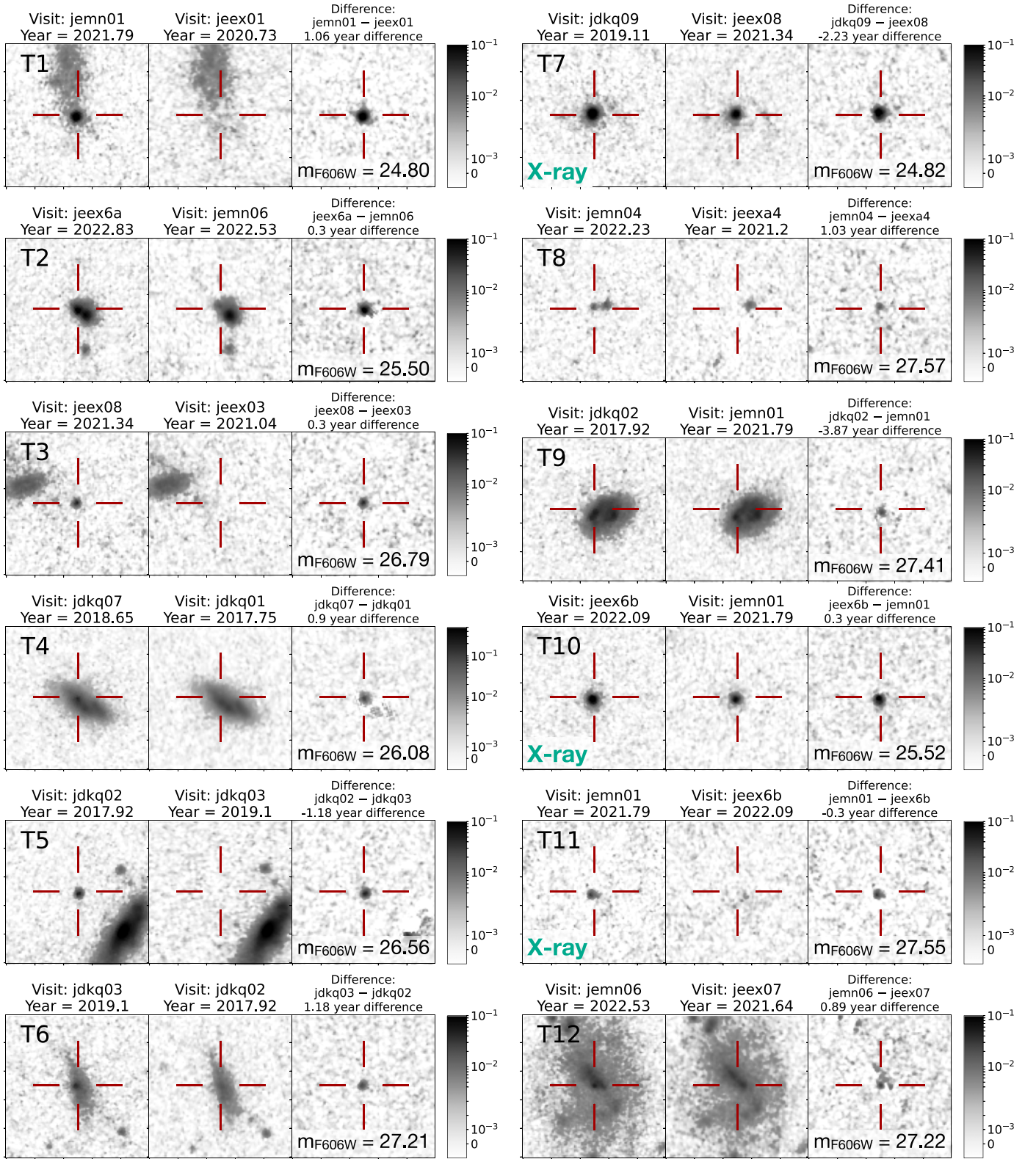
Figure 6. F606W images of each of the 12 transients identified within the JWST NEP TDF. For each transient we show a three-panel composite of 100×100 pixel ($3'' \times 3''$) cutouts from the image in which the transient is present (left), the image in which the transient is absent (middle), and the difference image (right). Labels give the transient ID, the visit IDs and dates of observation, the time interval between epochs, and the apparent F606W magnitude of the transient. Transients T7, T10, and T11 were also detected in X-rays (see Table 3), with T7 and T10 likely quasars. Grayscale bars to the right of each three-panel set are in units of e^- per second.

sources, but we expect typical 3σ upper limits of $\sim 1.4 \times 10^{-5}$ counts s^{-1} for the full 1.3 Ms exposure. For T7 and T10, we then extracted source fluxes using the `ciao` tool `srcflux` on the cross-registered event files for each OBSID. To convert

count rates to fluxes, we used a model with assumed Galactic absorption and a $\Gamma = 1.4$ power law. At $r \simeq 6\farcm5$ from the field center (characteristic of T7 and T10), this corresponds to 3σ upper limits of 3.2×10^{-16} erg s^{-1} cm^{-2}. Note, however, that

Table 2
Transients Identified in HST TREASUREHUNT Observations of the JWST NEP TDF

ID	R.A. (deg)	Decl. (deg)	Visit 1	Visit 2	t_1 (yr)	t_2 (yr)	Δt (yr)	m_{F435W} (mag)	m_{F606W} (mag)
T1	260.505468	65.798221	jemn01	jeex01	2021.789	2020.733	1.056	⋯	24.80 (0.05)
T2	260.585670	65.906841	jeex6a	jemn06	2022.830	2022.530	0.300	25.89 (0.29)	25.50 (0.09)
T3	260.835152	65.727517	jeex08	jeex03	2021.344	2021.035	0.309	⋯	26.79 (0.33)
T4	260.641524	65.883517	jdkq07	jdkq01	2018.647	2017.749	0.898	26.49 (0.59)	26.08 (0.16)
T5	260.618390	65.777831	jdkq02	jdkq03	2017.918	2019.101	−1.183	26.45 (0.52)	26.56 (0.26)
T6	260.602593	65.782095	jdkq03	jdkq02	2019.101	2017.918	1.183	⋯	27.21 (0.45)
T7	260.802040	65.725119	jdkq09	jeex08	2019.106	2021.344	−2.238	24.44 (0.08)	24.82 (0.05)
T8	260.967884	65.867384	jemn04	jeexa4	2022.227	2021.204	1.023	⋯	27.57 (0.67)
T9	260.544912	65.793210	jdkq02	jemn01	2017.918	2021.789	−3.871	⋯	27.41 (0.53)
T10	260.471298	65.762740	jeex6b	jemn01	2022.093	2021.789	0.304	25.59 (0.21)	25.52 (0.09)
T11	260.535175	65.763209	jemn01	jeex6b	2021.789	2022.093	−0.304	27.75 (1.70)	27.55 (0.66)
T12	260.501418	65.869263	jemn06	jeex07	2022.530	2021.637	0.893	⋯	27.22 (0.44)

Note. Columns (1)−(8) list the transient ID, the celestial coordinates (identified by eye) of the transient in decimal degrees, the root names of the visit where the transient is present (Visit 1) and where it is absent (Visit 2), the corresponding dates of observation, and the time interval Δt between Visits 1 and 2. The final two columns list the measured F435W and F606W magnitudes of the transient (m_{AB} at t_1 relative to t_2, measured within a circular aperture centered on the transient with a radius of 8 pixels), where the magnitude uncertainties are given in parentheses.

Table 3
Transients Identified in HST Observations of the JWST NEP TDF with Significant X-Ray Detections

Transient	Detected by	Flux (erg s^{-1} cm^{-2})	Band (keV)
T7	Chandra	$(5.36 \pm 0.64) \times 10^{-15}$	0.5–7
T7	XMM-Newton	$(1.41 \pm 0.41) \times 10^{-15}$	0.5–2
T7	XMM-Newton	$<9.03 \times 10^{-15}$	2–10
T10	Chandra	$(2.68 \pm 0.53) \times 10^{-15}$	0.5–7
T10	XMM-Newton	$(1.26 \pm 0.42) \times 10^{-15}$	0.5–2
T10	XMM-Newton	$<4.97 \times 10^{-15}$	2–10
T11	NuSTAR	$(1.14 \pm 0.41) \times 10^{-14}$	3–8

Note. Columns list the transient ID, the X-ray observatory that also detected the transient source, the measured X-ray flux, and the energy band in which that flux was measured. The XMM-Newton 2–10 keV upper limits correspond to the 90% confidence level.

the epochs of individual X-ray observations do not necessarily match or overlap with specific HST visits in which a transient was observed or absent.

4.1.2. Notes on Individual Transients

Transient T1 is detected only in F606W (although it is faintly discernible also in F435W) and appears in or superimposed on the outskirts of a diffuse, possibly clumpy disk galaxy, $\sim 1\rlap{.}''08$ S and $0\rlap{.}''16$ W of the estimated galaxy center. It has a red (F435W − F606W) color compared to the galaxy in a color-composite image, and its pointlike morphology and complete absence in Visit 2 (1.06 yr earlier) suggest that it is an SN within this $m_{F606W} \sim 23.9$ mag host galaxy.

Transient T2 is detected in both F606W and F435W and appears off-center in a centrally concentrated galaxy (possibly an elliptical galaxy) or in its fainter and partially overlapping apparent companion galaxy. It is located $\sim 0\rlap{.}''14$ E and $0\rlap{.}''09$ N of the core of the brighter ($m_{F606W} \sim 24.5$ mag) galaxy and closer in projected distance ($\sim 0\rlap{.}''07$ W and $0\rlap{.}''10$ S) to the center of the fainter one (not separately photometered by `SExtractor`). Its pointlike morphology and complete

absence in Visit 2 (0.30 yr earlier) suggest that it is an SN within either galaxy, with a visible color similar to that of its host.

Transient T3 is detected only in F606W. Its very red color is similar to that of a nearby extended disk galaxy or grouping of galaxies that is barely visible in F435W. Its pointlike morphology and complete absence in Visit 2 (0.31 yr earlier) suggest that it is an SN associated with this $m_{F606W} \sim 24.0$ mag host galaxy, appearing $\sim 1\rlap{.}''11$ W and $0\rlap{.}''32$ S of the center of the brightest region, although the relatively large separation from the main body of this potential host may allow different interpretations.

Transient T4 is detected in both F606W and F435W within an $m_{F606W} \sim 23.0$ mag disk galaxy with knots of apparent star formation and a secure MMT/Binospec spectroscopic redshift of $z = 0.615$. It appears $\sim 0\rlap{.}''10$ N and $0\rlap{.}''10$ E (a projected distance of ~ 1.0 kpc) of the estimated galaxy center, and its color is similar to that of the host. T4 appears pointlike and is completely absent in Visit 2 (0.90 yr earlier), but it is much fainter than its host galaxy, suggesting an SN caught either before or significantly past its peak brightness. T4 is currently the only transient with a spectroscopic redshift.

Transient T5 is detected in both F606W and F435W and appears well outside a nearby, highly inclined disk galaxy. It is located $\sim 0\rlap{.}''10$ E and $0\rlap{.}''01$ N of the core of that bright $m_{F606W} \sim 22.5$ mag galaxy, with a color that is similar or slightly bluer. No hint of this pointlike source is discernible in Visit 2 (1.18 yr later), suggesting that T5 may be an SN associated with the disk galaxy, although the relatively large separation from this potential host allows other interpretations.

Transient T6 is detected only in F606W (with perhaps a hint discernible in F435W) within a red and diffuse disk galaxy, $\sim 0\rlap{.}''09$ E and $0\rlap{.}''09$ N of the estimated galaxy center. It has a red color consistent with that of the galaxy, and its pointlike morphology and complete absence in Visit 2 (1.18 yr earlier) suggest that it is an SN within this $m_{F606W} \sim 24.4$ mag host galaxy.

Transient T7 is detected in both F606W and F435W and appears pointlike and isolated. It lacks any nearby potential host galaxy, although there may be a hint of signal $\sim 0\rlap{.}''59$ due E and due W and $\sim 0\rlap{.}''23$ due S, as well as some "fuzz" $\sim 0\rlap{.}''42$

to the NW in both Visits that could be due to a very faint potential host or galactic companions. Unlike most transients reported here, T7 is also clearly detected in Visit 2 (2.24 yr later) and has significant X-ray detections by both Chandra and XMM-Newton (see Table 3). This transient is thus unlikely to be an SN, but rather a quasar that exhibits significant variation in brightness.

Transient T8 is detected only in F606W and is our faintest transient at $m_{F606W} = 27.57$ mag. It appears $\sim 0.''27$ E and $0.''04$ S of a faint ($m_{F606W} \sim 27.3$ mag) and small nearby galaxy that may be similar in color, although possibly not quite as red. This point source is absent in Visit 2 (1.02 yr earlier), and the proximity to a potential host galaxy suggests that it could be an SN.

Transient T9 is detected only in F606W (although it is faintly discernible also in F435W) and appears in what looks like either a spiral arm of a relatively face-on disk galaxy or an interacting galaxy pair,[45] $\sim 0.''20$ E and $0.''08$ N of the estimated galaxy center. Its color is redder than that of an adjacent clump in the same spiral arm but is consistent with the color of most of the disk. Its pointlike morphology, projected location within a spiral arm, and absence in Visit 2 (3.87 yr later) suggest that T9 is a Type II SN associated with massive star formation within this $m_{F606W} \sim 23.4$ mag host galaxy.

Transient T10 is detected in both F606W and F435W, appears pointlike, and is isolated, lacking any nearby potential host galaxy. Unlike most transients reported here, T10 is also clearly detected in Visit 2 (0.30 yr earlier) and has significant X-ray detections by both Chandra and XMM-Newton (Table 3). This transient is thus unlikely to be an SN, but rather a quasar that exhibits significant variation in brightness.

Transient T11 is detected in both F606W and F435W, appears pointlike, and is isolated. The nearest galaxies are $\sim 2.''3$ to the S and $\sim 2.''6$ to the N, both >3 galaxy diameters away. Its color is relatively blue, allowing it to be clearly visible in F435W though $m_{F606W} = 27.55$ mag. This point source is absent in Visit 2 (0.30 yr later). Interestingly, T11 was detected with NuSTAR in the 3–8 keV band and thus is unlikely to be an SN.

Transient T12 is detected only in F606W and appears adjacent to a stellar bar across the center of an extended face-on spiral disk galaxy, $\sim 0.''12$ S and $0.''02$ E of the estimated galaxy center. Its color is redder than that bar but consistent with the color of other portions of the faint disk. Its pointlike morphology, projected location within the disk close to the central portions, and absence in Visit 2 (0.89 yr earlier) suggest that T12 is an SN within this $m_{F606W} \sim 22.5$ mag host galaxy.

The four brightest transients, T1, T2, T7, and T10, all of which are brighter than 25.6 mag, may be bright SNe or quasars. The significant X-ray detections of T7 and T10 specifically argue for the latter. In contrast, one of the faintest transients in this study, T11 with $m_{AB} \sim 27.5$ mag, is especially interesting, as it is the only transient without a potential host detected in F606W yet with noticeable X-ray emission.

4.2. Variability in the JWST NEP Time-domain Field

We identified 190 unique candidate variable candidates that meet the selection criteria of various samples discussed in Section 3.2, of which we estimate ~ 80 to be false positives (the

---

[45] A configuration resembling, e.g., NGC 5278/79 (Arp 239) or NGC 6050/IC 1179 (Arp 272).

exact number depends on how many false detections appeared in multiple variability samples). Figure 1 shows the locations of all 190 variable candidates. Symbol shapes (squares and diamonds) and hues identify the sample in which each variable was identified. Table 5 (at the end of this paper) provides a full list of IDs, celestial coordinates, data set IDs, and date of observation of each visit, as well as brightest measured apparent magnitude for each variable candidate. We also list the change in brightness between visits (in the sense Visit 2 − Visit 1) and the significance of variability in units of $\sigma_{\Delta m}$, for both the F435W and F606W filters.

We emphasize that we cannot claim any individual variable candidate varying at $<5\sigma_{\Delta m}$ significance to be a genuine variable. We can only place strong constraints on the overall number of variables in the area samples in a statistical sense. Conversely, we also do not exclude any specific sources as false detections from this final variability catalog, because we can only account for false positives in a statistical sense. We acknowledge that when an individual source is of interest, the source should be carefully analyzed and may require additional observations to ensure it is a genuine variable.

More relevant for population statistics, Table 4 lists the inferred number of genuine variable candidates, factoring in false detections, for different significance levels in either the F606W or F435W filters, or both. Figure 7 shows three-color composite cutouts for a representative sample of 12 variable candidates. The bottom row shows our most conservative sample of three galaxies that vary in both F435W and F606W at $\geqslant 3\sigma_{\Delta m}$ significance. Examples of variable sources drawn from the less restrictive samples are shown in the first three rows.

We estimate the total number of variable sources using the first, third, and fourth rows of Table 4, since variables in the second and fifth rows have more stringent selection criteria and are already included within these less restrictive samples. There are 206 objects listed in these specific rows of Table 4, where 16 are duplicates (i.e., matching more than one of these sample selection criteria), leaving 190 unique variable candidates. With an estimated ~ 80 false positives, this results in ~ 110 unique variable sources, or 0.42% of all 26,468 detected sources in the field. This is the maximum variable source fraction inferred in this work, as these samples are not necessarily independent. Our most conservative sample of $\geqslant 3\sigma_{\Delta m}$ variable objects in both F435W and F606W only makes up 0.02% of the parent population.

We also estimate the areal density of variable sources using the total number of inferred genuine variables. These ~ 110 unique variable candidates translate to ~ 1.25 variables arcmin^{-2} (~ 4500 deg^{-2}) of overlapping area. We can therefore expect ~ 14 new variable sources per additional fully overlapping ACS/WFC footprint (~ 11.3 arcmin^2), assuming F606W imaging to similar depths to the TREASUREHUNT observations.

The $3\sigma_{\Delta m}$ threshold, which determines by what magnitude a galaxy must vary to be flagged as variable, is key to putting our findings in context with other work. Higher noise levels naturally result in fewer detected galaxies, so the threshold helps to normalize these variations. The solid brown curves in Figure 3 show the $1\sigma_{\Delta m}$, $2\sigma_{\Delta m}$, and $3\sigma_{\Delta m}$ thresholds (for the F606W filter) as a function of magnitude. For all sources with $m_{0.24} \sim 26.0$ mag (a 1.0 mag wide bin centered on 26.0 mag), the median $3\sigma_{\Delta m}$ threshold is $\Delta m_{0.24} = 0.14$ mag. In other
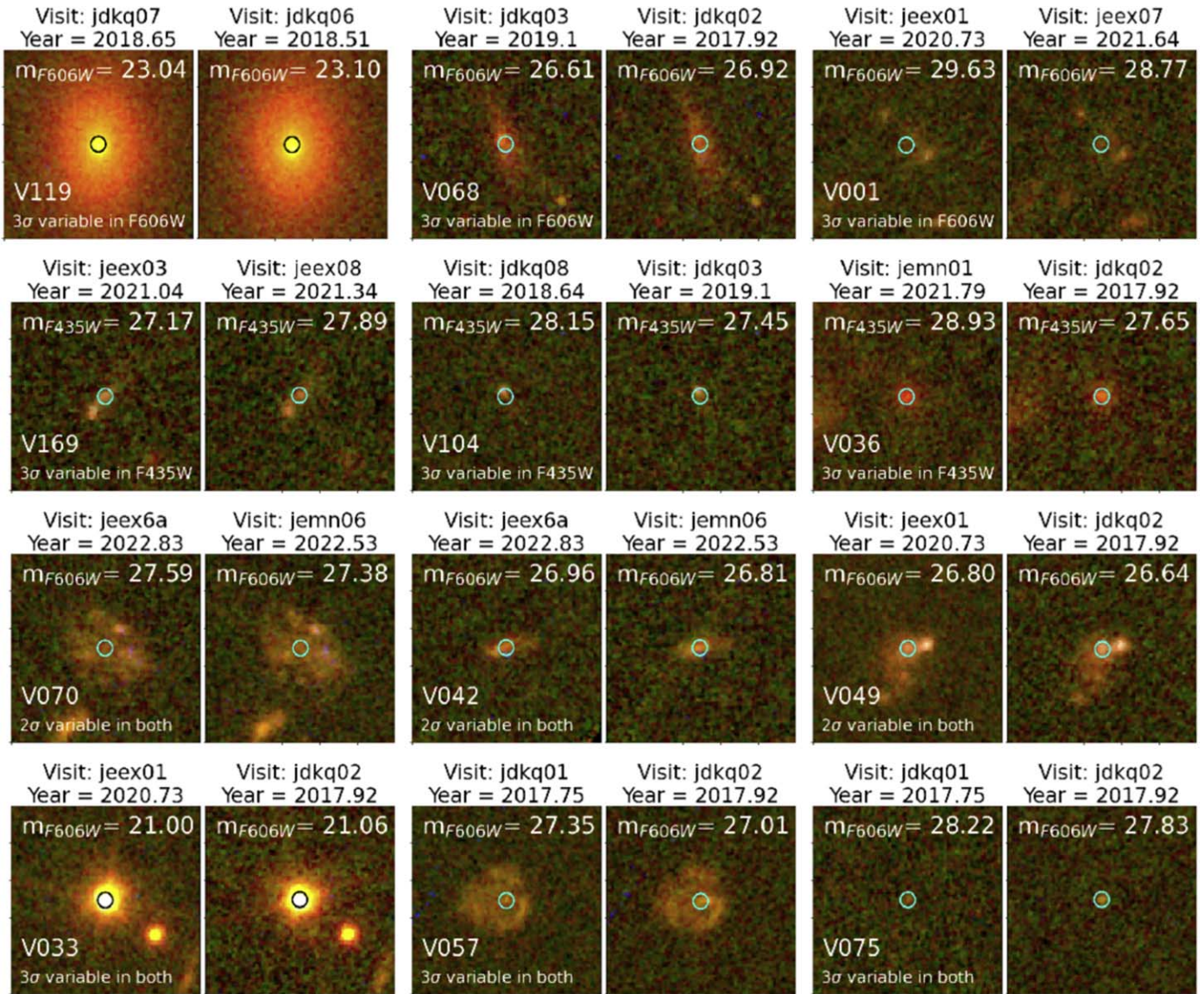
Figure 7. Color composites of 12 representative variable candidates, with F606W, F435W, and F275W shown in red, green, and blue hues, respectively. Each row of 100×100 pixel ($3'' \times 3''$) cutouts corresponds to a different sample: (1) F606W-only $3\sigma_{\Delta m}$, (2) F435W-only $3\sigma_{\Delta m}$, (3) F435W and F606W $2\sigma_{\Delta m}$, and (4) F435W and F606W $3\sigma_{\Delta m}$ variability. A cyan or black circle at the center of each cutout represents the $0''\!.24$ aperture in which variability was detected. Above each cutout, we note the visit identifier and decimal year of observation. At the top of each cutout, we include the measured $m_{0.24}$ magnitude for that visit. In the left panel of each pair of cutouts, at the bottom, we list the variable candidate identification number and whether it is variable in the F606W filter, the F435W filter, or both. Most of the variable candidates will be AGNs, although some will be faint or obscured SNe.

Table 4
Number of Variable Candidates Identified and Inferred in F606W and F435W

Sample	All Objects	Apparent Variables	False Positives	Inferred Variables	% Variable
F606W ($3\sigma_{\Delta m}$)	26,468	145	48	97	0.37%
F606W ($5\sigma_{\Delta m}$)	26,468	10	0	10	0.04%
F435W ($3\sigma_{\Delta m}$)	13,574	23	18	5	0.04%
F606W and F435W ($2\sigma_{\Delta m}$)	13,574	38	13	25	0.18%
F606W and F435W ($3\sigma_{\Delta m}$)	13,574	3	<1	3	0.02%

Note. Columns list the sample of variable candidates, with the significance limit given between parentheses; the total number of sources in the parent sample, limited to the F435W parent sample in the case of a combined F606W+F435W selection; the number of objects satisfying the criteria at face value; the number of false-positive detections expected; the number of genuine variable sources after statistical correction for false positives; and the inferred percentage of sources in the parent sample that are variable.

words, a typical 26.0 mag source would need to vary by at least 0.14 mag to be flagged as variable for this specific data set. For bins centered on 27.0 and 28.0 mag, the $3\sigma_{\triangle m}$ thresholds are 0.24 and 0.41 mag, respectively. For the F435W filter, the $3\sigma_{\triangle m}$ thresholds for bins centered on 26.0, 27.0, and 28.0 mag are 0.26, 0.44, and 0.82 mag, respectively.

Although our variability identification pipeline was developed to identify variable AGNs, we still detect 6 out of the 12 transients presented in Section 4.1. Specifically, it identifies transients T2, T3, T5, T6, T9, and T11. Transients T7 and T10 were originally identified to exhibit variability, but they were flagged and removed as star candidates owing to their small FWHM. Transients T1, T4, T8, and T12 did not satisfy the $3\sigma_{\triangle m}$ threshold owing to their relatively large photometric uncertainties.

4.3. Photometric Redshift Estimation and SED Fits

To gain a better understanding of the transients and variable candidates in the field, we estimated photometric redshifts using EAZY (Brammer et al. 2008). This specifically allows us to understand the distances of the variable candidates and to explore various properties of them, such as their masses, ages, dust extinction, and specific star formation rates (sSFRs).

Since that would be impossible with just the three HST filters, we also used PEARLS JWST/NIRCam images (see Section 2). Consequently, we estimate redshifts only for the subset of galaxies that fall within the overlapping coverage of both HST and JWST. We opted not to use the HST F275W filter for photometric redshift estimations, because most objects remain undetected at sufficient significance. We thus employed a total of 10 filters for estimating photometric redshifts: HST/ACS F435W and F606W, and JWST/NIRCam F090W, F115W, F150W, F200W, F277W, F356W, F410M, and F444W. To ensure that the HST and JWST images are on the same pixel scale, we reprojected each HST image onto the PEARLS F444W image pixel grid using reproject. In each filter, we set all pixels without coverage in all 10 filters to NaN values, facilitating flagging of objects at image edges.

We created photometric catalogs for input into EAZY using SExtractor. Recognizing that some galaxies exhibit variability that may bias a redshift estimation, we ran SExtractor on HST drizzled images of each individual visit instead of the full HST mosaic, and we use the measurement with the fainter flux. We assume that the fainter measurement represents the photometry if no variability was present—galaxies may temporarily brighten, but they cannot get dimmer on human timescales. For the JWST data, we used the full mosaics, since only a single epoch yet exists at any given location within the field. The NIRCam F444W image served as the SExtractor detection image in all cases. For HST images, we set MAG_ZEROPOINT to 26.49 mag for F606W and to 25.65 mag for F435W. For our JWST images, MAG_ZEROPOINT was set to 28.0865 mag for all filters, as appropriate for their $0''030$ plate scale, to convert from MJy sr^{-1} (see Windhorst et al. 2023). Other relevant parameters are the same for HST and JWST and are as listed in the rightmost column of Table 1.

EAZY (v1.0) was run on the resulting 10-band photometry. Following the approach outlined in Figure 3, we scale SExtractor magnitude uncertainties by a factor of 3 upon input into EAZY. This factor of 3 is larger than the factor of 1.15 used for scaling the $0''24$ aperture magnitudes in

Section 3.2, primarily due to the larger aperture sizes used here. We used the eazy_v1.0 templates on a redshift grid spanning $0.01 \leqslant z \leqslant 15$, allowing only single templates to be fit. We adopted z_ml as the redshift estimate and did not include any priors.

We used the EAZY redshifts as input to a custom IDL SED fitting code that was also recently used by Meinke et al. (2021, 2023). This code starts with Bruzual & Charlot (2003, hereafter BC03) SED models assuming a Salpeter initial mass function (IMF) and an exponentially decaying star formation history specified by the decay scale, τ, which ranges from 0.01 to 100 Gyr in 16 logarithmically spaced steps. Extinction by dust is specified on a grid of $0.0\,\text{mag} \leqslant A_V \leqslant 4.0\,\text{mag}$ in steps of 0.2 mag assuming a Calzetti et al. (2000) extinction law. For a given redshift, the age, T, is not allowed to exceed the age of the Universe (assuming a Planck Collaboration et al. 2020 cosmology). The best-fit model is chosen by minimizing the χ^2 and scaling for the stellar mass, M. The (unweighted) present-day value of the star formation rate, $\Psi(T)$, is computed using the best-fit stellar mass, decay scale (τ), and age (T) from $\Psi(T) = \Psi_0 e^{-T/\tau}$, where Ψ_0 is the star formation rate at time $T = 0$. Given that $M = \int_0^T \Psi(t)\,dt$, we can solve Ψ_0 analytically from $\Psi_0 = (M/\tau)/(1 - e^{-T/\tau})$.

With 10-band, 0.4–5 μm photometry, we required $\chi^2 < 10$ and $z < 5.5$. Since all objects of interest are detected in F606W, they must be at $z < 5.5$. However, these cuts alone will not eliminate all bad fits, especially if the photometric uncertainties in some crucial filters are large. We added an additional condition that the limits on the 2σ confidence interval in redshift probability distribution, $p(z)$, as computed by EAZY (namely l95 and u95) must not differ by more than 1 redshift unit. These conditions result in a sample with reliable photometric redshift estimates that includes 22 galaxies exhibiting variability (28% of the original sample of 79 variables that fall within the HST and JWST footprints) and 3296 normal galaxies (31% of the 10,664 galaxies that fall within the HST and JWST footprints). We only considered galaxies that were already marked as reliable in Section 3.2.1 (the 26,468 sources in Table 4).

Due to the necessarily limited grid of SED model parameters, any galaxy with an inferred sSFR $< 10^{-5}\,\text{yr}^{-1}$ is categorized as "quiescent," and its sSFR is set to $10^{-5}\,\text{yr}^{-1}$. Our templates also cannot distinguish stellar population ages younger than 10 Myr, so we set all apparent age solutions <0.01 Gyr to 0.01 Gyr. Given that age is inversely correlated with the inferred sSFR, where $\log_{10}(\text{Age}) \sim -2$ corresponds to $\log_{10}(\text{sSFR}) \sim 2$, we also set all $\log_{10}(\text{sSFR}) > 2$ to 2. This adjustment is solely made to assess collective trends in galaxies with variability.

In Figure 8, we compare photometric redshift (z_{ph}), stellar mass, stellar population age, sSFR, and dust extinction (A_V) of galaxies that exhibit variability to those of typical galaxies in the general population. Overall, we sample a broad range of redshifts, masses, ages, star formation histories, and dust extinction. The most prominent peaks in the fraction of galaxies with variability with respect to the general galaxy population (expressed in %) occur at a redshift of $z_{\text{ph}} \simeq 2.5$, a stellar mass of $\sim 10^8$ and $\sim 10^{10}\,M_\odot$, an age of $\sim 10^{-0.5}$ Gyr, an sSFR of $\sim 10^{-5}\,\text{Gyr}^{-1}$, and an attenuation $A_V \simeq 1.0$ mag. The median redshift of our variability sample is $z_{\text{ph}} = 1.3$, but we sample variability up to $z_{\text{ph}} = 2.9$. Similarly, our galaxies with variability sample masses $M = (0.02–20) \times 10^9\,M_\odot$, ages $T = 0.01–2$ Gyr, sSFR $= 10^{-5}$ to $10^2\,\text{Gyr}^{-1}$, and $A_V = 0.0–2.4$ mag.
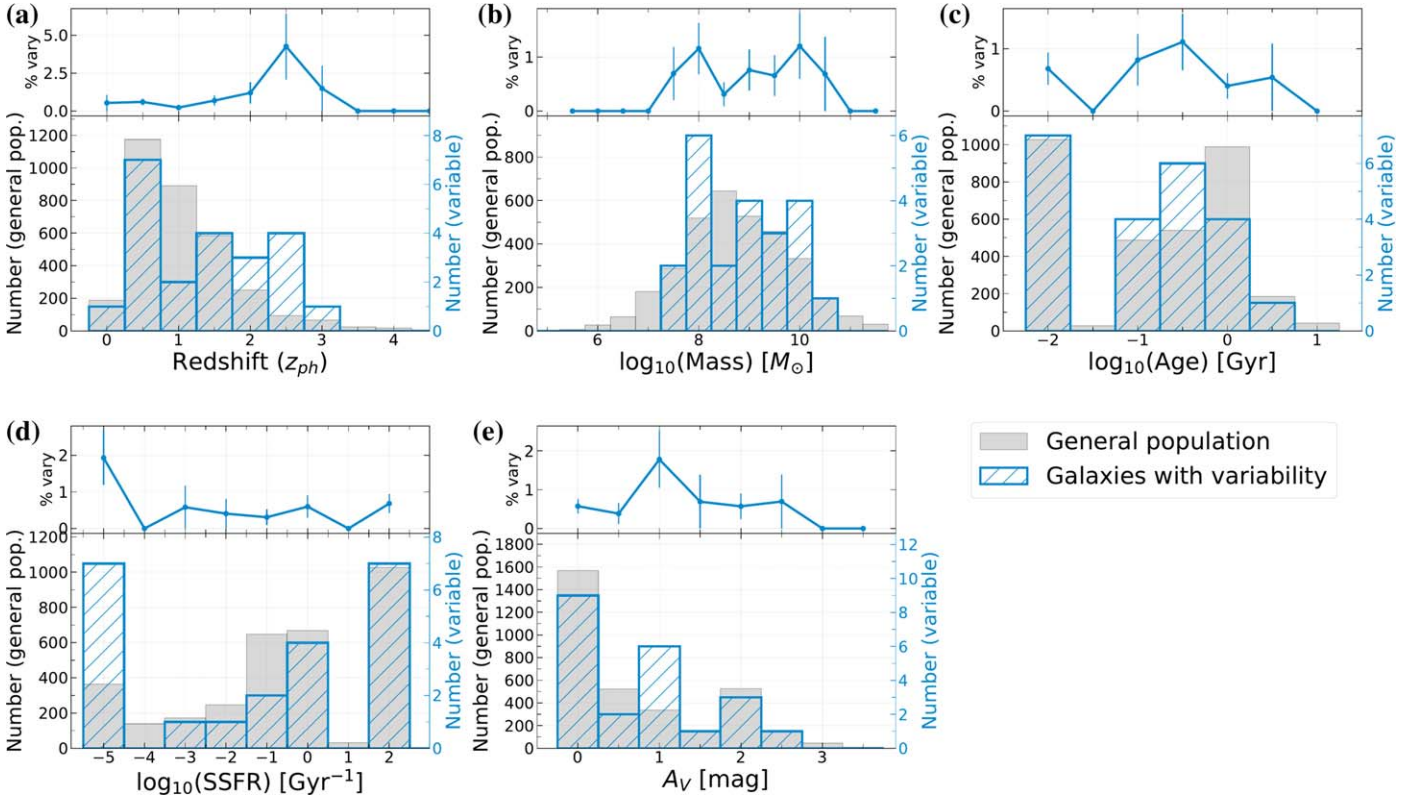
Figure 8. Comparison of galaxy properties in the general galaxy population and in galaxies that exhibit variability. Shown are distributions of (a) photometric redshifts (z_{ph}), (b) stellar mass, (c) stellar population age, (d) sSFR, and (e) extinction by dust (A_V), for the general population (solid gray) and galaxies with variability (blue hatched). The y-axis labels on the left-hand side of each plot represent the number of galaxies in the general population, and those on the right-hand side (in blue) represent the number of galaxies with variability. Above each histogram panel, we plot the fraction of galaxies with variability ($100\% \times N_{var}/N_{general}$) for each bin. The uncertainties assume Poisson statistics with $\sigma_N \propto \sqrt{N}$. This comparison only includes the subset of galaxies already flagged as reliable in Section 3.2.1, with both HST and JWST imaging (where photometric redshifts and SEDs can be fit), with $z_{ph} < 5.5$, $\chi^2 < 10$, and where the 2σ confidence interval in $p(z)$ spans <1 redshift unit.

Three transients fell within an area that also has PEARLS eight-filter JWST/NIRCam coverage, yet all three had EAZY photometric redshifts with a $\chi^2 > 10$. This could be due to a significant nonthermal component from an AGN, or to the presence of strong emission lines that could mimic a continuum break. As transient T4 has a secure MMT/Binospec spectroscopic redshift of $z = 0.615$, we used the Code Investigating GALaxy Emission (CIGALE; Boquien et al. 2019) to better fit the SED of its host galaxy. CIGALE has the benefit of incorporating emission lines into its models, while the previously mentioned SED fitting algorithm does not and resulted in poorer fits for this transient host. We used a delayed burst–quench star formation history model (Ciesla et al. 2017), since the standard exponentially declining model can struggle to reproduce higher SFRs, and its morphology suggests that the transient host likely underwent a recent star formation episode. The e-folding times tested were 1, 3, 5, and 8 Gyr, the main stellar population spanned 1–8 Gyr in increments of 1 Gyr, the burst/quench age ranged from 0.1 to 1 Gyr, and the possible SFR ratios before and after these burst ages were 0.1, 0.3, and 0.6. Our stellar component used the BC03 library using the Salpeter IMF, testing metallicities of 0.004, 0.02, and 0.05 $Z_\odot$, with young stellar ages being either 10 or 100 Myr. We included a nebular component to account for emission lines using all the default parameters, where the nebular component is self-consistent with the stellar population in the sense that its strength is determined by the Lyman continuum of the total SED. To account for dust attenuation, we used Calzetti et al.

(2000) extinction with possible modified power-law slopes of -0.4, 0.2, and 0. For dust *emission*, we used the Dale et al. (2014) model with α slopes of 1.0, 2.0, and 3.0.

The best-fit SED for the T4 host galaxy is shown in Figure 9 and corresponds to a stellar population age of 3.6 Gyr, $A_V = 0.5$ mag of attenuation by dust, and a stellar mass of $1.2 \times 10^{10} M_\odot$. Its sSFR is 0.5 $M_\odot$ Gyr^{-1}. The reported best-fit value of 0.05 of the reduced χ^2 indicates that the (conservative) photometric uncertainties upon input to CIGALE were overestimating the actual ones somewhat.

5. Discussion

An analysis of the detailed properties of individual transients and variable candidates is beyond the scope of this paper. We can, however, make some general statements about the properties of these source populations, using their observed optical light distributions (morphology) and EAZY SED fits. From the pointlike morphology and off-center locations at small projected distances to likely host galaxies, we infer that the majority of the discovered transients are SNe. The majority of the variable candidates, on the other hand, are found either in or very near the center of galaxies or are isolated without a discernible host, and they are surmised to be AGNs. Most of these AGNs are normal SMBHs in galaxies, with stochastically fluctuating accretion at lower luminosities than seen in quasars. Nonetheless, it is important to consider that other phenomena, such as SNe from central starbursts, stochastic microlensing
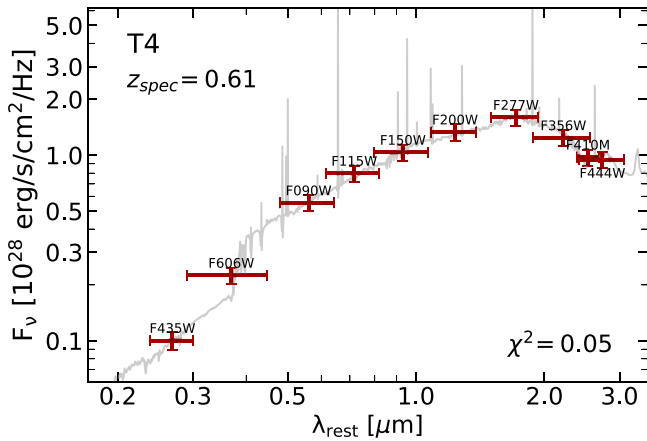
Figure 9. SED fit of transient T4 with CIGALE, adopting the MMT/Binospec spectroscopic redshift of 0.615. The red points with vertical error bars show the measured fluxes of the transient host and their associated uncertainties. The horizontal bars on each data point represent the width of the bandpass. The light-gray spectrum represents the best CIGALE fit, with the reduced χ^2 value shown.

events, and tidal disruption events, could also contribute to the observed central variability. SNe that are heavily obscured and SNe that are caught at very early times or at late times can contribute to variability detected in local peaks in surface brightness well away from host galaxy centers.

5.1. Classification of Transients

Based on their positions relative to likely host galaxies and the PSF-like appearance in the difference images, we propose that nine of the transients (T1, T2, T3, T4, T5, T6, T8, T9, and T12) are SNe. It is reasonable to expect that ~40%–50% of detected SNe are Type Ia, as suggested by previous studies (Dahlen et al. 2012; Graur et al. 2014; Rodney et al. 2014; Cappellaro et al. 2015). If we assume that we have a minimum of nine SNe, we can anticipate a minimum of three Type Ia SNe, with the remainder being CC SNe.

The TREASUREHUNT observing strategy provided piece-meal UV–visible imaging rather than time-domain monitoring. As a result, these SN candidates will have long faded and can no longer be followed up for spectroscopic identification. None-theless, now that this initial imaging exists, future monitoring observations could efficiently expand the present sample and would allow such spectroscopic follow-up. The sum of the areas of overlap used in this work samples ~88 arcmin², which is about half of the total HST coverage of this field (~194 arcmin²). Therefore, we can expect about $2\times$ as many transients if this field were observed again. Full overlapping coverage of this field could yield at least six new Type Ia SNe and, coupled with spectra and rapid follow-up, can provide essential constraints on fundamental cosmological parameters like the Hubble constant, the mass density of the Universe, the cosmological constant, the deceleration parameter, and the age of the Universe (e.g., Riess et al. 1998, 2023). In addition to Type Ia SNe, comprehensive HST coverage of this field could yield at least six CC SN observations. Particularly when combined with ancillary data, this could contribute significantly to resolving the observed discrepancies in CC SN rates compared to theoretical models (Cappellaro 2014). With a sufficiently large sample, the SN rate as a function of redshift could also be constrained. Furthermore, the increased volume of observations enhances the likelihood of

capturing rare or unexpected events, potentially leading to groundbreaking discoveries in the field.

At least three of the transients are unlikely to be SNe. They either were detected in both epochs or are isolated with no apparent host galaxy. When considering only the optical emission, transients T7 and T10 exhibit substantial changes in brightness between the two epochs, of $\Delta m = 0.83 \pm 0.06$ mag and 0.82 ± 0.09 mag, respectively. That would be equivalent to the presence of an additional source with $m_{AB} \sim 24.82$ and 25.52 mag. The observed centroid positions in both epochs match to within $0\rlap{.}{''}001$, such that the additional signal is indistinguishable from being due to a nuclear source that changed brightness. We therefore suggest that T7 and T10 may be quasars. The fact that they both were detected in soft X-rays at flux levels $>2 \times 10^{-15}$ erg s^{-1} cm^{-2} lends additional evidence to this interpretation.

T11 is a unique transient with no visible host, yet it was detected in hard X-rays by NuSTAR. If that X-ray emission is indeed associated with T11, then it could be a faint ($m_{AB} \gtrsim 29$ mag), high-redshift quasar that briefly flared up to be detectable in F606W. If the X-ray emission is unrelated, then we speculate that T11 may represent an SN located within an undetected host galaxy. That host could be a faint dwarf galaxy at $z \lesssim 6$, or a more massive host at $z \gtrsim 6$ to explain the nondetection in F606W in the second visit. Unfortunately, T11 falls outside the area with JWST coverage, so we cannot distinguish between these two scenarios at this time. Chakrabarti et al. (2018) have demonstrated that the rates of SNe in dwarf galaxies can be three times higher (per unit volume) than in typical spiral galaxies. Given the limited understanding of star formation in dwarf galaxies, a substantial number of SN candidates like T11 could offer a unique opportunity to identify otherwise undetected dwarf galaxies and gain more insights into their star formation rates.

Overall, determining the nature of each transient remains challenging without spectroscopic data secured close in time. Nonetheless, these detected events showcase the considerable potential and effectiveness of transient science within the JWST NEP TDF.

5.2. Properties of Variable Candidates

Our methods were developed to isolate variable candidates that are coincident with local maxima in surface brightness that can be isolated and photometered using SExtractor. This naturally optimizes detection of variable AGNs, but faint SNe are also detected when located offset from the center of the host galaxy. In addition, some offset variability may also be due to accretion disks of SMBHs that have not yet settled in the center of the host galaxy (e.g., Reines et al. 2020). Examples of offset variables are shown in Figure 7 (objects V001 and V169).

In general, the number of variable sources inferred here is expected to be fewer than the true number in the field, as some sources will vary on timescales that were not probed in this work. Constructing a sample of genuine variable sources in the field requires follow-up observations at various time sampling intervals, possibly extending over decades.

Figure 8 shows that galaxies exhibiting variability span a broad range of stellar mass, stellar population age, star formation history, and dust extinction. This underscores that rest-frame UV–visible variability can be a powerful tactic to identify accreting AGNs in a wide cross section of the galaxy population. Especially notable is that AGNs were detected

through their variability even in dusty galaxies with $A_V \gtrsim 2$ mag.

The top portion of each panel in Figure 8, of the fraction of galaxies with variability within each histogram bin for the quantity plotted, shows peaks in most of the panels, although the formal significance of these peaks (assuming Poisson counting statistics) is generally $\lesssim 2\sigma$ owing to small number statistics in individual bins.

First, in Figure 8(a), we find a relatively high fraction of galaxies with variability around $z \sim 2.5$, while at both lower and higher redshifts variability appears to be rarer. This is in contrast with both Villforth et al. (2012), who find optical–near-infrared variable AGNs predominantly toward lower redshifts, and Sarajedini et al. (2011), who find an increase in optically varying AGNs with increasing redshift. Zhong et al. (2022) find a similar number of optically variable AGNs to peak at $z \sim 1$. We suspect that the number of variable sources as a function of redshift is influenced by cosmic variance of a relatively rare source population and thus differs depending on the field observed. The fraction of variable sources may be flat over the $0 \lesssim z \lesssim 3$ redshift range when averaged over an area of sufficient size.

The observed stellar mass distribution (Figure 8(b)) of galaxies exhibiting variability shows an apparent excess at both $\sim 10^8$ and $\sim 10^{10} M_\odot$. We do not detect variability in the most massive galaxies, either due to small number statistics (most likely) or because their SMBHs are less likely to accrete at a sufficient rate to be detectable or have a longer period of relative quiescence between major accretion events. We also do not detect variability in galaxies with $M \lesssim 10^7 M_\odot$, likely due to a combination of both small number statistics and larger photometric uncertainties in these faint systems, such that our $3\sigma_{\Delta m}$ threshold is less likely to be met for a given amplitude of variability. If the relative distribution is taken at face value, then it could also hint at the presence of two separate populations of sources with variability: one associated with lower-mass ($\sim 10^8 M_\odot$) hosts, and another associated with higher-mass ($\sim 10^{10} M_\odot$) hosts. Such could be the case if variability associated with CC SNe favors lower-mass host galaxies and variability associated with Type Ia SNe and AGNs favors higher-mass hosts.

In Figures 8(c) and (d) we see that a significant fraction of the galaxies with variability are best fit with stellar population models characterized by active star formation (young ages $\lesssim 30$ Myr and high sSFR $\gtrsim 30$ Gyr^{-1}). Conversely, there is also a sizable fraction that is quiescent (sSFR $\lesssim 0.01$ Gyr^{-1}) with stellar populations older than 1 Gyr. A possible excess appears for intermediate population ages (60–600 Myr).

Lastly, Figure 8(e) shows that while the galaxies exhibiting variability largely track the distribution of extinction seen in the general population, there may be an excess in the variability sample for $A_V \sim 1$ mag.

5.3. Constraints on SMBH Mass, Accretion, and Radiation Lifetimes

The sparse and random time sampling of this field does not allow us to trace the evolution of faint AGNs but may still teach us about various properties of them. AGN brightness varies on timescales corresponding to the light-crossing time in the accretion disks and gas clouds surrounding SMBHs. For example, for an SMBH with a mass $M \sim 10^8 M_\odot$, the timescale for variability cannot be shorter than ~ 1 week in the rest frame

(e.g., Xie et al. 2005). For the majority of sources where the variability is due to AGN activity, that variability originates close to the central SMBH. If the timescale we sample is the minimum timescale of variation, we can provide rough constraints on the SMBH masses following Xie et al. (2005). According to Schwarzschild black hole theory (SBHT), the mass of a black hole ($M_\bullet$ in $M_\odot$) is equal to the minimum timescale of variation ($\Delta t_{\min}$ in years) as $M_\bullet = 4.29 \times 10^{11} \Delta t_{\min}$. Time intervals between observations in various areas of overlap in the TREASUREHUNT data range from 1 day (0.0027 yr) to 4.78 yr. At the median redshift of our variable candidate sample, $z_{ph} = 1.3$, the range in rest-frame timescales becomes 0.001–2.08 yr, giving SMBH masses of $5.1 \times 10^8 M_\odot \lesssim M_\bullet \lesssim 8.9 \times 10^{11} M_\odot$. SMBH masses $\gtrsim 10^{11} M_\odot$ are unreasonable: objects within the region of overlap with a 4.78 yr interval between observations likely vary on much shorter timescales, and we did not sample the minimum timescale of variation. Even a more typical time interval of ~ 1 yr between epochs will yield a $\sim 10^{11} M_\odot$ SMBH mass. Taking the full range in redshifts sampled into account, we will therefore claim that only in select areas of overlap can we probe SMBHs with masses of $M_\bullet \gtrsim (3-9) \times 10^8 M_\odot$, but with no firm upper limit.

We can also frame our finding that a maximum of 0.42% of the general field galaxy population shows significant variability in the context of the accretion and radiation lifetimes of AGN. If we assume that (1) all galaxies seen in this field with HST have a central SMBH (e.g., Kormendy & Ho 2013), (2) the central SMBH is always visible when accreting, and (3) a currently accreting AGN will be variable, then we would deduce that the AGNs in our field are actively accreting for 0.42% of the time. Assumptions 2 and 3 are simplified, as some AGNs will be hidden at rest-frame UV–visible wavelengths by surrounding dust. This fraction could be as large as 2/3 of all AGNs, if we use the $\sim 30\%$ average Lyman continuum escape fraction of weak AGNs (Smith et al. 2018, 2020, 2024) as a proxy for the fraction of AGNs with direct unobscured sight lines to the observer. Figure 8(c) implies an average SED age of $\sim 10^8$ yr (~ 100 Myr) for the parent population, although the spread in age is wide (0.01–10 Gyr). A 0.42% fraction of visibly variable AGNs would correspond to an implied average AGN activity lifetime of $0.42\% \times 10^8 \sim 4 \times 10^5$ yr (and a range of 4×10^4 to 4×10^7 yr). For comparison, Rawes et al. (2015) estimated the optical synchrotron electron lifetimes of AGNs with visible jets observed with HST and Chandra at $\sim 10^4$ yr. However, they state that their estimated synchrotron lifetimes may be too short by at least a factor of 2 and may be longer if synchrotron electrons are reaccelerated in the ambient magnetic field. On the other end of the activity scale, Jakobsen et al. (2003) show that at least some quasars can remain active more or less continuously for $\gtrsim 10$ Myr. With these assumptions and significant uncertainties, a visible AGN accretion time of $\sim 10^4$–10^7 yr could indeed result in a 0.42% variability fraction in a galaxy population characterized by an average SED age of ~ 100 Myr (and a range of 0.01–10 Gyr) whose stars and gas feed that central engine.

Future work will need to secure and analyze larger samples of optically variable sources with deep X-ray imaging to better constrain UV–visible synchrotron lifetimes and wider and deeper HST+JWST images with spectroscopic (NIRISS or NIRSpec) redshifts to improve redshifts and the characterization of their stellar population.

Table 5
Variable Sources Identified in HST TREASUREHUNT Observations of the JWST NEP TDF

ID	CatID	R.A. (deg)	Decl. (deg)	Visit 1	Visit 2	t_1 (yr)	t_2 (yr)	Δt (yr)	$m_{0.24}$ (mag)	$\Delta m_{0.24}$ (mag)	$\sigma_{\Delta m}$	$m_{0.24}$ (mag)	$\Delta m_{0.24}$ (mag)	$\sigma_{\Delta m}$
(1)	(2)	(3)	(4)	(5)	(6)	(7)	(8)	(9)	(10)	(11)	(12)	(13)	(14)	(15)
V001	19364	260.4052851	65.8382044	jeex01	jeex07	2020.733	2021.637	−0.904	28.86 (0.34)	−0.83	1.79	28.77 (0.21)	−0.86	3.64
V002	19815	260.4300229	65.8342205	jeex01	jeex07	2020.733	2021.637	−0.904	28.84 (0.47)	−0.74	1.17	28.69 (0.33)	1.15	3.04
V003	19785	260.4326188	65.8345545	jeex01	jeex07	2020.733	2021.637	−0.904	27.93 (0.24)	0.79	2.40	28.00 (0.15)	0.55	3.23
V004	20003	260.4473218	65.8318503	jeex01	jeex07	2020.733	2021.637	−0.904	28.65 (0.40)	0.68	1.27	28.23 (0.17)	0.59	3.04
V005	41428	260.4502146	65.7515390	jemn01	jeex6b	2021.789	2022.093	−0.304	29.10 (0.50)	0.43	0.63	28.84 (0.33)	1.13	3.00
V006	20130	260.4604344	65.8296368	jeex01	jeex07	2020.733	2021.637	−0.904	28.33 (0.46)	1.37	2.20	28.75 (0.23)	0.62	2.36
V007	20104	260.4622684	65.8300200	jeex01	jeex07	2020.733	2021.637	−0.904	27.49 (0.15)	0.56	2.74	27.49 (0.09)	0.28	2.84
V008	40135	260.4800396	65.7615899	jemn01	jeex6b	2021.789	2022.093	−0.304	28.97 (0.68)	0.93	1.02	28.67 (0.30)	1.05	3.10
V009	42426	260.4811656	65.7389668	jemn01	jeex6b	2021.789	2022.093	−0.304	24.68 (0.03)	−0.12	3.13	23.39 (0.01)	−0.04	2.97
V010	48837	260.4847004	65.8816131	jemn06	jeex07	2022.530	2021.637	0.893	27.92 (0.28)	−0.81	2.17	27.65 (0.10)	−0.26	2.14
V011	48800	260.4850911	65.8819144	jemn06	jeex07	2022.530	2021.637	0.893	27.17 (0.13)	−0.19	1.09	28.66 (0.36)	−1.29	3.12
V012	48831	260.4857008	65.8816066	jemn06	jeex07	2022.530	2021.637	0.893	27.92 (0.28)	−0.81	2.17	28.55 (0.32)	1.23	3.33
V013	48977	260.4903910	65.8782280	jemn06	jeex07	2022.530	2021.637	0.893	28.33 (0.26)	−0.35	1.02	28.29 (0.19)	0.77	3.52
V014	39334	260.4918589	65.7687739	jemn01	jeex6b	2021.789	2022.093	−0.304	28.75 (0.33)	−0.06	0.13	28.52 (0.22)	0.81	3.24
V015	48934	260.4943736	65.8797585	jemn06	jeex07	2022.530	2021.637	0.893	28.53 (0.41)	0.68	1.24	28.22 (0.17)	0.59	3.07
V016	19975	260.4965078	65.8309014	jeex01	jeex07	2020.733	2021.637	−0.904	19.18 (0.01)	0.03	7.62	19.46 (0.03)	0.13	3.42
V017	49160	260.4965104	65.8742828	jemn06	jeex07	2022.530	2021.637	0.893	28.43 (0.26)	0.12	0.36	28.03 (0.13)	0.47	3.14
V018	42276	260.4979360	65.7417349	jemn01	jeex6b	2021.789	2022.093	−0.304	28.77 (0.35)	−0.04	0.08	28.57 (0.23)	−0.81	3.03
V019	40970	260.5045403	65.7556663	jemn01	jeex6b	2021.789	2022.093	−0.304	28.12 (0.33)	0.89	2.03	29.00 (0.34)	0.92	2.37
V020	39013	260.5060240	65.7731007	jemn01	jeex6b	2021.789	2022.093	−0.304	28.86 (0.41)	−0.08	0.14	27.98 (0.13)	0.57	3.71
V021	38120	260.5075136	65.7925038	jemn01	jdkq02	2021.789	2017.918	3.871	29.06 (0.64)	−0.83	0.96	28.74 (0.29)	1.13	3.37
V022	38237	260.5090095	65.7913053	jemn01	jdkq02	2021.789	2017.918	3.871	28.63 (0.32)	−0.01	0.02	28.31 (0.17)	0.60	3.05
V023	17632	260.5109164	65.8123441	jeex01	jdkq02	2020.733	2017.918	2.815	28.90 (0.43)	−0.45	0.76	28.61 (0.26)	0.89	3.01
V024	38331	260.5132040	65.7883638	jemn01	jdkq02	2021.789	2017.918	3.871	28.16 (0.44)	1.24	2.09	28.79 (0.24)	0.62	2.22
V025	17466	260.5132587	65.8165789	jeex01	jdkq02	2020.733	2017.918	2.815	27.85 (0.28)	−1.16	3.07	29.40 (0.35)	−0.42	1.06
V026	17481	260.5139809	65.8162782	jeex01	jdkq02	2020.733	2017.918	2.815	27.85 (0.28)	−1.16	3.07	29.28 (0.37)	0.71	1.66
V027	17482	260.5148620	65.8162530	jeex01	jdkq02	2020.733	2017.918	2.815	27.85 (0.28)	−1.16	3.07	28.13 (0.13)	−0.28	1.95
V028	42324	260.5156057	65.7410733	jemn01	jeex6b	2021.789	2022.093	−0.304	28.62 (0.34)	0.16	0.36	27.34 (0.09)	0.35	3.45
V029	49278	260.5165718	65.8723986	jemn06	jeex07	2022.530	2021.637	0.893	29.37 (0.51)	0.01	0.02	28.17 (0.18)	−0.86	4.10
V030	39884	260.5168553	65.7637201	jemn01	jeex6b	2021.789	2022.093	−0.304	29.02 (0.59)	0.66	0.83	28.04(0.15)	−0.58	3.43
V031	17642	260.5181754	65.8119968	jeex01	jdkq02	2020.733	2017.918	2.815	25.73 (0.05)	0.01	0.11	25.52 (0.03)	0.23	5.72
V032	41667	260.5200938	65.7490569	jemn01	jeex6b	2021.789	2022.093	−0.304	28.80 (0.43)	−0.36	0.61	28.59 (0.28)	1.02	3.14
V033	17861	260.5203993	65.8073115	jeex01	jdkq02	2020.733	2017.918	2.815	21.56 (0.01)	−0.04	4.18	21.00 (0.01)	0.06	14.72
V034	17017	260.5285670	65.8336403	jeex01	jdkq02	2020.733	2017.918	2.815	25.52 (0.04)	−0.01	0.15	24.85 (0.02)	0.09	3.37
V035	17815	260.5286942	65.8079924	jeex01	jdkq02	2020.733	2017.918	2.815	28.89 (0.41)	0.32	0.58	28.12 (0.15)	0.61	3.58
V036	37564	260.5290447	65.8045199	jemn01	jdkq02	2021.789	2017.918	3.871	27.65 (0.29)	−1.28	3.28	26.37 (0.05)	0.01	0.25
V037	39503	260.5295628	65.7668789	jemn01	jeex6b	2021.789	2022.093	−0.304	27.11 (0.12)	−0.24	1.47	28.53 (0.27)	−1.14	3.63
V038	37829	260.5301461	65.7975577	jemn01	jdkq02	2021.789	2017.918	3.871	28.69 (0.40)	−0.50	0.92	28.40 (0.19)	0.68	3.10
V039	40938	260.5321327	65.7559458	jemn01	jeex6b	2021.789	2022.093	−0.304	28.72 (0.68)	−1.23	1.34	28.58 (0.25)	−0.90	3.18
V040	5015	260.5324664	65.8591989	jdkq01	jeex07	2017.749	2021.637	−3.888	24.38 (0.03)	0.07	2.13	22.35 (0.01)	−0.07	8.83
V041	37499	260.5337585	65.8079004	jemn01	jdkq02	2021.789	2017.918	3.871	24.84 (0.03)	−0.08	1.79	23.51 (0.01)	0.08	5.92
V042	33111	260.5339889	65.9156836	jeex6a	jemn06	2022.830	2022.530	0.300	27.20 (0.14)	−0.40	2.20	26.81 (0.06)	−0.15	2.09
V043	40338	260.5343798	65.7602481	jemn01	jeex6b	2021.789	2022.093	−0.304	29.16 (0.52)	−0.11	0.16	28.08 (0.14)	−0.49	3.07
V044	39949	260.5351364	65.7631956	jemn01	jeex6b	2021.789	2022.093	−0.304	27.97 (0.25)	0.41	1.21	27.69 (0.19)	1.27	5.95
V045	17127	260.5351702	65.8285103	jeex01	jdkq02	2020.733	2017.918	2.815	29.56 (0.59)	−0.11	0.14	28.62 (0.25)	0.88	3.05

Table 5
(Continued)

ID	CatID	R.A. (deg)	Decl. (deg)	Visit 1	Visit 2	t_1 (yr)	t_2 (yr)	Δt (yr)	$m_{0.24}$ (mag)	$\Delta m_{0.24}$ (mag)	$\sigma_{\Delta m}$	$m_{0.24}$ (mag)	$\Delta m_{0.24}$ (mag)	$\sigma_{\Delta m}$
(1)	(2)	(3)	(4)	(5)	(6)	(7)	(8)	(9)	(10)	(11)	(12)	(13)	(14)	(15)
V046	41298	260.5354508	65.7527669	jemn01	jeex6b	2021.789	2022.093	−0.304	28.75 (0.43)	−0.42	0.73	27.86 (0.14)	0.57	3.58
V047	38098	260.5366516	65.7930824	jemn01	jdkq02	2021.789	2017.918	3.871	28.25 (0.27)	0.31	0.86	28.17 (0.16)	0.72	3.86
V048	39683	260.5391875	65.7652426	jemn01	jeex6b	2021.789	2022.093	−0.304	28.13 (0.25)	−0.34	0.98	28.60 (0.28)	−1.05	3.25
V049	17165	260.5419552	65.8281206	jeex01	jdkq02	2020.733	2017.918	2.815	26.82 (0.10)	−0.34	2.63	26.64 (0.06)	−0.16	2.42
V050	38172	260.5436430	65.7915235	jemn01	jdkq02	2021.789	2017.918	3.871	28.01 (0.26)	0.79	2.20	27.80 (0.11)	0.48	3.79
V051	38266	260.5439886	65.7895398	jemn01	jdkq02	2021.789	2017.918	3.871	29.64 (0.73)	−0.22	0.23	28.69 (0.25)	0.86	3.03
V052	17831	260.5441742	65.8076230	jeex01	jdkq02	2020.733	2017.918	2.815	28.48 (0.38)	−0.85	1.67	28.73 (0.33)	1.16	3.06
V053	38122	260.5449020	65.7931821	jemn01	jdkq02	2021.789	2017.918	3.871	26.56 (0.08)	−0.03	0.26	25.82 (0.04)	−0.21	4.62
V054	39765	260.5451659	65.7641522	jemn01	jeex6b	2021.789	2022.093	−0.304	29.01 (0.54)	0.58	0.80	28.54 (0.24)	−0.91	3.30
V055	40721	260.5457177	65.7587033	jemn01	jeex6b	2021.789	2022.093	−0.304	28.12 (0.32)	−0.87	2.01	28.31 (0.17)	−0.49	2.54
V056	37972	260.5485168	65.7954958	jemn01	jdkq02	2021.789	2017.918	3.871	28.55 (0.31)	−0.16	0.38	28.41 (0.30)	1.42	4.11
V057	48	260.5548528	65.8386224	jdkq01	jdkq02	2017.749	2017.918	−0.169	27.15 (0.12)	−0.49	3.00	27.01 (0.07)	−0.34	4.06
V058	33274	260.5610833	65.9123618	jeex6a	jemn06	2022.830	2022.530	0.300	28.39 (0.41)	0.82	1.47	28.21 (0.18)	0.66	3.23
V059	32938	260.5613045	65.9189714	jeex6a	jemn06	2022.830	2022.530	0.300	29.43 (0.64)	0.16	0.19	28.50 (0.22)	−0.78	3.11
V060	6238	260.5683705	65.7831566	jdkq03	jdkq02	2019.101	2017.918	1.183	28.78 (0.46)	0.52	0.84	27.37 (0.09)	−0.36	3.35
V061	41126	260.5686500	65.7542573	jemn01	jeex6b	2021.789	2022.093	−0.304	28.31 (0.42)	1.15	2.01	28.27 (0.15)	0.36	2.05
V062	33539	260.5688549	65.9067578	jeex6a	jemn06	2022.830	2022.530	0.300	29.17 (0.57)	−0.40	0.52	28.29 (0.17)	0.62	3.13
V063	33524	260.5855449	65.9068262	jeex6a	jemn06	2022.830	2022.530	0.300	25.57 (0.05)	0.16	2.27	25.41 (0.03)	0.21	5.59
V064	34022	260.5865160	65.8956540	jeex6a	jemn06	2022.830	2022.530	0.300	22.45 (0.01)	−0.07	4.92	29.03 (0.22)	−0.06	0.23
V065	234	260.5868385	65.8333537	jdkq01	jdkq02	2017.749	2017.918	−0.169	28.37 (0.23)	−0.08	0.25	28.32 (0.18)	−0.71	3.40
V066	6629	260.5886084	65.7776747	jdkq03	jdkq02	2019.101	2017.918	1.183	28.05 (0.25)	0.59	1.71	28.74 (0.24)	0.89	3.17
V067	320	260.5901557	65.8318573	jdkq01	jdkq02	2017.749	2017.918	−0.169	23.25 (0.01)	0.02	1.05	21.70 (0.01)	0.02	3.63
V068	6334	260.6025353	65.7820869	jdkq03	jdkq02	2019.101	2017.918	1.183	27.59 (0.15)	−0.05	0.23	26.61 (0.06)	0.30	4.42
V069	34339	260.6027231	65.8860494	jeex6a	jemn06	2022.830	2022.530	0.300	28.42 (0.38)	0.98	1.89	28.79 (0.30)	1.08	3.11
V070	34133	260.6032077	65.8928444	jeex6a	jemn06	2022.830	2022.530	0.300	27.61 (0.18)	−0.55	2.28	27.38 (0.08)	−0.21	2.21
V071	34238	260.6051718	65.8906921	jeex6a	jemn06	2022.830	2022.530	0.300	29.87 (0.82)	0.07	0.07	28.70 (0.24)	−0.85	3.09
V072	6269	260.6061960	65.7821730	jdkq03	jdkq02	2019.101	2017.918	1.183	24.62 (0.03)	−0.02	0.50	23.86 (0.02)	−0.07	4.09
V073	3339	260.6121812	65.8528375	jdkq01	jdkq07	2017.749	2018.647	−0.898	28.75 (0.32)	0.21	0.48	28.12 (0.16)	0.61	3.38
V074	6605	260.6177291	65.7775875	jdkq03	jdkq02	2019.101	2017.918	1.183	25.31 (0.04)	−0.06	1.01	24.53 (0.02)	−0.10	4.11
V075	663	260.6220866	65.8272493	jdkq01	jdkq02	2017.749	2017.918	−0.169	27.68 (0.20)	−0.86	3.24	27.83 (0.11)	−0.40	3.01
V076	5684	260.6225709	65.7904307	jdkq03	jdkq02	2019.101	2017.918	1.183	27.92 (0.31)	1.02	2.45	28.44 (0.17)	0.46	2.42
V077	1294	260.6246197	65.8807391	jdkq01	jdkq07	2017.749	2018.647	−0.898	27.98 (0.20)	−0.53	2.01	28.03 (0.12)	−0.40	2.81
V078	3134	260.6252980	65.8542599	jdkq01	jdkq07	2017.749	2018.647	−0.898	28.44 (0.27)	−0.21	0.59	28.13 (0.15)	−0.53	3.05
V079	11949	260.6257482	65.8157473	jdkq08	jdkq02	2018.645	2017.918	0.727	28.87 (0.42)	−0.61	1.09	28.43 (0.22)	−0.98	3.89
V080	5284	260.6287600	65.7986047	jdkq03	jdkq02	2019.101	2017.918	1.183	29.42 (0.68)	−0.30	0.32	28.78 (0.31)	−1.18	3.33
V081	32136	260.6292399	65.8979164	jeex6a	jdkq07	2022.830	2018.647	4.183	27.79 (0.21)	0.76	2.67	26.81 (0.06)	0.18	2.51
V082	11609	260.6327010	65.8281680	jdkq08	jdkq02	2018.645	2017.918	0.727	28.59 (0.27)	−0.36	0.99	28.56 (0.19)	−0.67	3.09
V083	2974	260.6335344	65.8561320	jdkq01	jdkq07	2017.749	2018.647	−0.898	23.61 (0.02)	−0.01	0.60	21.91 (0.01)	−0.02	3.69
V084	4711	260.6350207	65.8290677	jdkq01	jdkq08	2017.749	2018.645	−0.896	28.87 (0.36)	−0.32	0.67	28.61 (0.31)	−1.23	3.46
V085	2872	260.6381441	65.8573742	jdkq01	jdkq07	2017.749	2018.647	−0.898	28.66 (0.35)	−0.57	1.21	28.37 (0.17)	0.62	3.07
V086	5236	260.6391309	65.7993893	jdkq03	jdkq02	2019.101	2017.918	1.183	26.39 (0.07)	0.04	0.37	24.53 (0.02)	0.09	4.18
V087	31994	260.6421239	65.9029309	jeex6a	jdkq07	2022.830	2018.647	4.183	23.99 (0.02)	−0.01	0.26	22.26 (0.01)	0.03	4.12
V088	1426	260.6421779	65.8780433	jdkq01	jdkq07	2017.749	2018.647	−0.898	28.76 (0.29)	0.15	0.37	28.51 (0.20)	0.76	3.24
V089	4463	260.6460086	65.8377478	jdkq01	jdkq08	2017.749	2018.645	−0.896	28.77 (0.28)	0.01	0.02	28.51 (0.24)	−0.91	3.29
V090	3860	260.6476671	65.8447077	jdkq01	jdkq07	2017.749	2018.647	−0.898	29.00 (0.40)	0.35	0.64	28.77 (0.35)	−1.20	3.01

Table 5
(Continued)

ID	CatID	R.A. (deg)	Decl. (deg)	Visit 1	Visit 2	t_1 (yr)	t_2 (yr)	Δt (yr)	$m_{0.24}$ (mag)	$\Delta m_{0.24}$ (mag)	$\sigma_{\Delta m}$	$m_{0.24}$ (mag)	$\Delta m_{0.24}$ (mag)	$\sigma_{\Delta m}$
(1)	(2)	(3)	(4)	(5)	(6)	(7)	(8)	(9)	(10)	(11)	(12)	(13)	(14)	(15)
V091	12341	260.6578804	65.8123865	jdkq08	jdkq03	2018.645	2019.101	−0.456	28.23 (0.35)	−1.02	2.15	27.85 (0.11)	−0.28	2.22
V092	2939	260.6676957	65.8565418	jdkq01	jdkq07	2017.749	2018.647	−0.898	28.10 (0.21)	0.33	1.17	28.23 (0.17)	0.58	3.03
V093	12870	260.6677285	65.7981739	jdkq08	jdkq03	2018.645	2019.101	−0.456	28.88 (0.36)	−0.06	0.13	27.54 (0.09)	−0.33	3.14
V094	4423	260.6680216	65.8388153	jdkq01	jdkq08	2017.749	2018.645	−0.896	27.10 (0.10)	0.06	0.43	28.63 (0.25)	0.90	3.13
V095	2469	260.6684303	65.8631755	jdkq01	jdkq07	2017.749	2018.647	−0.898	29.23 (0.43)	0.09	0.15	28.24 (0.33)	−1.57	4.18
V096	12868	260.6747247	65.7980539	jdkq08	jdkq03	2018.645	2019.101	−0.456	28.62 (0.43)	−0.86	1.48	28.49 (0.24)	−0.88	3.22
V097	48064	260.6753285	65.9216637	jemn05	jeex6a	2022.377	2022.830	−0.453	28.21 (0.22)	0.01	0.04	28.63 (0.24)	−0.89	3.16
V098	15034	260.6772860	65.8538229	jdkq08	jdkq07	2018.645	2018.647	−0.002	28.04 (0.19)	0.09	0.36	28.10 (0.15)	0.68	3.84
V099	3932	260.6794726	65.8408931	jdkq01	jdkq07	2017.749	2018.647	−0.898	29.21 (0.49)	0.58	0.88	28.13 (0.14)	0.49	3.09
V100	48124	260.6803062	65.9204980	jemn05	jeex6a	2022.377	2022.830	−0.453	28.10 (0.20)	0.15	0.57	28.17 (0.16)	−0.69	3.82
V101	15545	260.6815935	65.8449714	jdkq08	jdkq07	2018.645	2018.647	−0.002	28.85 (0.33)	0.22	0.50	28.48 (0.21)	0.76	3.23
V102	12867	260.6822444	65.7979657	jdkq08	jdkq03	2018.645	2019.101	−0.456	26.89 (0.10)	−0.24	1.78	28.72 (0.26)	0.94	3.17
V103	48474	260.6830765	65.9131667	jemn05	jeex6a	2022.377	2022.830	−0.453	27.95 (0.29)	−0.98	2.53	28.17 (0.14)	−0.42	2.51
V104	12872	260.6845500	65.7978732	jdkq08	jdkq03	2018.645	2019.101	−0.456	27.45 (0.17)	−0.70	3.11	27.60 (0.09)	−0.09	0.85
V105	7585	260.6923363	65.7739049	jdkq04	jdkq03	2018.221	2019.101	−0.880	28.17 (0.26)	−0.61	1.74	28.44 (0.21)	−0.95	3.88
V106	12912	260.6948845	65.7964272	jdkq08	jdkq03	2018.645	2019.101	−0.456	23.61 (0.02)	−0.17	6.58	23.30 (0.01)	0.01	0.88
V107	46007	260.6995990	65.7123076	jemn02	jdkq09	2021.940	2019.106	2.834	26.96 (0.09)	−0.01	0.06	24.36 (0.02)	0.08	3.83
V108	44457	260.7055562	65.7256191	jemn02	jdkq09	2021.940	2019.106	2.834	27.12 (0.11)	0.19	1.27	26.52 (0.05)	0.19	3.21
V109	44621	260.7056172	65.7226130	jemn02	jdkq09	2021.940	2019.106	2.834	28.16 (0.40)	−1.14	2.11	28.63 (0.24)	−0.86	3.15
V110	7638	260.7078911	65.7730268	jdkq04	jdkq03	2018.221	2019.101	−0.880	28.83 (0.55)	−1.05	1.43	28.64 (0.26)	0.95	3.22
V111	45164	260.7102095	65.7169415	jemn02	jdkq09	2021.940	2019.106	2.834	28.80 (0.40)	0.32	0.59	28.38 (0.27)	1.36	4.32
V112	13412	260.7123985	65.7927245	jdkq08	jdkq04	2018.645	2018.221	0.424	27.84 (0.16)	−0.20	0.93	26.91 (0.06)	−0.25	3.47
V113	45918	260.7167982	65.7087560	jemn02	jdkq09	2021.940	2019.106	2.834	27.88 (0.21)	−0.16	0.60	26.49 (0.05)	0.19	3.11
V114	7098	260.7175478	65.7848453	jdkq04	jdkq03	2018.221	2019.101	−0.880	24.53 (0.03)	−0.01	0.41	22.81 (0.01)	0.03	3.23
V115	45686	260.7192384	65.7123368	jemn02	jdkq09	2021.940	2019.106	2.834	27.88 (0.25)	−0.73	2.20	27.82 (0.12)	−0.37	2.78
V116	8197	260.7200109	65.7631919	jdkq04	jdkq03	2018.221	2019.101	−0.880	24.17 (0.02)	−0.02	0.57	23.40 (0.01)	0.06	4.30
V117	44851	260.7250941	65.7203820	jemn02	jdkq09	2021.940	2019.106	2.834	28.83 (0.40)	−0.05	0.10	28.32 (0.19)	−0.67	3.07
V118	11469	260.7287189	65.8579825	jdkq07	jdkq06	2018.647	2018.511	0.136	28.35 (0.34)	0.89	1.94	28.38 (0.19)	0.73	3.36
V119	10689	260.7358381	65.8754246	jdkq07	jdkq06	2018.647	2018.511	0.136	24.60 (0.03)	0.04	0.91	23.04 (0.01)	0.06	5.33
V120	44649	260.7372179	65.7239799	jemn02	jdkq09	2021.940	2019.106	2.834	28.27 (0.24)	−0.09	0.28	28.01 (0.15)	−0.53	3.07
V121	45250	260.7375391	65.7161188	jemn02	jdkq09	2021.940	2019.106	2.834	28.80 (0.50)	−0.64	0.96	28.77 (0.31)	1.09	3.07
V122	44894	260.7383881	65.7200561	jemn02	jdkq09	2021.940	2019.106	2.834	28.63 (0.33)	−0.13	0.29	28.11 (0.16)	0.56	3.16
V123	44048	260.7396362	65.7294908	jemn02	jdkq09	2021.940	2019.106	2.834	27.74 (0.18)	−0.21	0.86	28.57 (0.26)	−1.09	3.60
V124	43264	260.7454366	65.7380214	jemn02	jdkq09	2021.940	2019.106	2.834	19.25 (0.01)	0.07	13.92	19.50 (0.02)	−0.33	13.27
V125	16264	260.7488596	65.7509596	jdkq09	jdkq04	2019.106	2018.221	0.885	28.41 (0.28)	0.44	1.16	28.54 (0.21)	−0.72	3.03
V126	44831	260.7505188	65.7205403	jemn02	jdkq09	2021.940	2019.106	2.834	27.61 (0.29)	−1.18	3.01	27.89 (0.12)	−0.11	0.77
V127	45380	260.7514847	65.7150048	jemn02	jdkq09	2021.940	2019.106	2.834	27.73 (0.23)	−0.75	2.37	27.51 (0.10)	−0.24	2.15
V128	43642	260.7545349	65.7350399	jemn02	jdkq09	2021.940	2019.106	2.834	28.56 (0.32)	0.29	0.67	28.30 (0.16)	0.55	3.04
V129	15975	260.7564058	65.7560911	jdkq09	jdkq04	2019.106	2018.221	0.885	29.24 (0.46)	0.07	0.11	28.32 (0.20)	0.72	3.16
V130	42985	260.7569328	65.7430011	jemn02	jdkq09	2021.940	2019.106	2.834	27.87 (0.21)	0.58	2.01	27.85 (0.11)	0.34	2.67
V131	43199	260.7654001	65.7398784	jemn02	jdkq09	2021.940	2019.106	2.834	29.29 (0.59)	0.21	0.26	28.63 (0.28)	1.02	3.22
V132	44494	260.7709607	65.7242314	jemn02	jdkq09	2021.940	2019.106	2.834	28.30 (0.30)	−0.44	1.10	28.32 (0.18)	−0.68	3.33
V133	43060	260.7745589	65.7419473	jemn02	jdkq09	2021.940	2019.106	2.834	28.12 (0.28)	0.72	1.90	28.35 (0.17)	0.62	3.13
V134	45001	260.7764730	65.7187770	jemn02	jdkq09	2021.940	2019.106	2.834	26.10 (0.06)	−0.05	0.55	25.65 (0.03)	0.12	3.04
V135	9852	260.7809939	65.8383387	jdkq06	jdkq05	2018.511	2018.363	0.148	27.94 (0.21)	0.46	1.63	27.63 (0.10)	0.39	3.45

Table 5
(Continued)

ID	CatID	R.A. (deg)	Decl. (deg)	Visit 1	Visit 2	t_1 (yr)	t_2 (yr)	Δt (yr)	$m_{0.24}$ (mag)	$\Delta m_{0.24}$ (mag)	$\sigma_{\Delta m}$	$m_{0.24}$ (mag)	$\Delta m_{0.24}$ (mag)	$\sigma_{\Delta m}$
(1)	(2)	(3)	(4)	(5)	(6)	(7)	(8)	(9)	(10)	(11)	(12)	(13)	(14)	(15)
V136	9811	260.7820403	65.8390785	jdkq06	jdkq05	2018.511	2018.363	0.148	27.51 (0.14)	0.17	0.93	28.53 (0.19)	0.70	3.18
V137	45900	260.7829845	65.7089929	jemn02	jdkq09	2021.940	2019.106	2.834	28.00 (0.26)	0.64	1.83	28.06 (0.14)	0.49	3.03
V138	16432	260.7838837	65.7488263	jdkq09	jdkq04	2019.106	2018.221	0.885	28.42 (0.38)	−0.86	1.70	28.48 (0.21)	0.74	3.12
V139	46426	260.7901866	65.7007683	jemn02	jdkq09	2021.940	2019.106	2.834	28.16 (0.22)	0.00	0.01	27.59 (0.10)	−0.43	3.74
V140	8862	260.7966543	65.8514172	jdkq06	jdkq05	2018.511	2018.363	0.148	25.51 (0.05)	−0.08	1.30	25.35 (0.03)	−0.11	3.06
V141	31209	260.7976797	65.7264133	jeex08	jdkq09	2021.344	2019.106	2.238	29.20 (0.55)	−0.57	0.76	28.40 (0.22)	0.88	3.53
V142	9654	260.8007573	65.8408780	jdkq06	jdkq05	2018.511	2018.363	0.148	27.83 (0.20)	0.48	1.82	28.65 (0.26)	0.98	3.34
V143	28674	260.8063693	65.8799829	jeex05	jdkq06	2021.347	2018.511	2.836	28.27 (0.20)	0.44	1.59	27.76 (0.09)	0.36	3.44
V144	30070	260.8105090	65.7371529	jeex08	jdkq09	2021.344	2019.106	2.238	27.49 (0.15)	−0.18	0.88	28.05 (0.15)	0.54	3.16
V145	30045	260.8122328	65.7373452	jeex08	jdkq09	2021.344	2019.106	2.238	28.47 (0.47)	−1.10	1.73	28.71 (0.35)	1.23	3.04
V146	8477	260.8163753	65.7965563	jdkq05	jdkq04	2018.363	2018.221	0.142	26.81 (0.09)	−0.02	0.18	26.36 (0.05)	−0.21	3.53
V147	30059	260.8219253	65.7371863	jeex08	jdkq09	2021.344	2019.106	2.238	28.63 (0.45)	0.76	1.25	28.27 (0.22)	1.14	4.52
V148	28638	260.8274735	65.8806602	jeex05	jdkq06	2021.347	2018.511	2.836	28.37 (0.23)	−0.15	0.48	28.00 (0.14)	0.49	3.09
V149	22712	260.8347912	65.7296116	jeex03	jdkq09	2021.035	2019.106	1.929	28.36 (0.27)	0.06	0.16	28.32 (0.17)	0.62	3.10
V150	27404	260.8352185	65.7275413	jeex03	jeex08	2021.035	2021.344	−0.309	29.01 (0.70)	−0.69	0.73	27.38 (0.24)	−2.08	7.53
V151	47730	260.8358472	65.8893731	jemn04	jeex05	2022.227	2021.347	0.880	28.32 (0.30)	0.86	2.10	28.52 (0.22)	1.10	4.33
V152	9712	260.8429092	65.8400901	jdkq06	jdkq05	2018.511	2018.363	0.148	28.72 (0.34)	−0.39	0.85	28.68 (0.25)	0.93	3.24
V153	23869	260.8442446	65.7597401	jeex03	jeex08	2021.035	2021.344	−0.309	28.85 (0.39)	0.30	0.57	28.69 (0.29)	−1.10	3.27
V154	47372	260.8451666	65.8991518	jemn04	jeex05	2022.227	2021.347	0.880	28.80 (0.68)	−0.83	0.90	28.77 (0.33)	−1.21	3.17
V155	47667	260.8468371	65.8914197	jemn04	jeex05	2022.227	2021.347	0.880	27.66 (0.25)	1.03	3.01	27.96 (0.12)	0.28	2.04
V156	22013	260.8477623	65.7413624	jeex03	jdkq09	2021.035	2019.106	1.929	28.30 (0.47)	1.24	1.96	28.61 (0.25)	0.92	3.23
V157	25243	260.8539353	65.7457044	jeex03	jeex08	2021.035	2021.344	−0.309	27.75 (0.32)	1.33	3.12	28.44 (0.17)	−0.06	0.33
V158	25240	260.8541929	65.7458702	jeex03	jeex08	2021.035	2021.344	−0.309	27.75 (0.32)	1.33	3.12	27.48 (0.09)	−0.06	0.59
V159	30067	260.8578555	65.7371669	jeex08	jdkq09	2021.344	2019.106	2.238	28.25 (0.26)	−0.48	1.37	28.07 (0.13)	0.48	3.16
V160	27723	260.8600711	65.7221800	jeex03	jeex08	2021.035	2021.344	−0.309	24.03 (0.02)	−0.03	1.06	21.98 (0.01)	−0.03	4.86
V161	22223	260.8619972	65.7380793	jeex03	jdkq09	2021.035	2019.106	1.929	28.21 (0.27)	0.64	1.73	28.34 (0.16)	−0.72	3.79
V162	9531	260.8638246	65.8420120	jdkq06	jdkq05	2018.511	2018.363	0.148	29.46 (0.63)	−0.51	0.59	28.70 (0.27)	1.01	3.25
V163	24676	260.8653220	65.7504766	jeex03	jeex08	2021.035	2021.344	−0.309	28.42 (0.51)	−0.97	1.41	28.40 (0.20)	0.71	3.09
V164	25310	260.8719766	65.7454975	jeex03	jeex08	2021.035	2021.344	−0.309	28.54 (0.33)	0.22	0.50	28.03 (0.16)	−0.67	3.68
V165	24248	260.8746031	65.7549045	jeex03	jeex08	2021.035	2021.344	−0.309	27.52 (0.20)	−0.67	2.49	27.00 (0.07)	−0.22	2.64
V166	24737	260.8778166	65.7497988	jeex03	jeex08	2021.035	2021.344	−0.309	26.33 (0.09)	−0.40	3.27	26.27 (0.05)	−0.07	1.31
V167	47239	260.8785658	65.9050944	jemn04	jeex05	2022.227	2021.347	0.880	27.33 (0.18)	0.65	2.73	27.16 (0.08)	0.22	2.40
V168	24124	260.8799575	65.7558947	jeex03	jeex08	2021.035	2021.344	−0.309	27.77 (0.58)	−1.77	2.26	27.29 (0.08)	−0.24	2.55
V169	27313	260.8844831	65.7282510	jeex03	jeex08	2021.035	2021.344	−0.309	27.17 (0.15)	0.71	3.44	27.25 (0.08)	0.11	1.29
V170	26382	260.8880858	65.7366434	jeex03	jeex08	2021.035	2021.344	−0.309	28.41 (0.30)	0.34	0.86	28.54 (0.23)	0.93	3.44
V171	25315	260.8883667	65.7454453	jeex03	jeex08	2021.035	2021.344	−0.309	27.37 (0.17)	0.75	3.26	27.35 (0.08)	0.08	0.92
V172	24771	260.8931970	65.7496619	jeex03	jeex08	2021.035	2021.344	−0.309	29.00 (0.64)	−0.69	0.80	28.65 (0.27)	−1.03	3.32
V173	36203	260.8957973	65.8157113	jeexa4	jdkq05	2021.204	2018.363	2.841	28.61 (0.28)	0.34	0.87	28.36 (0.16)	0.59	3.32
V174	36152	260.8966926	65.8174593	jeexa4	jdkq05	2021.204	2018.363	2.841	26.22 (0.06)	−0.01	0.17	23.86 (0.01)	0.21	12.76
V175	36188	260.8977353	65.8156259	jeexa4	jdkq05	2021.204	2018.363	2.841	25.16 (0.04)	−0.02	0.37	24.81 (0.02)	0.08	3.17
V176	36219	260.8981358	65.8157672	jeexa4	jdkq05	2021.204	2018.363	2.841	25.49 (0.05)	−0.04	0.65	25.26 (0.03)	0.11	3.22
V177	36471	260.9048765	65.8670380	jeexa4	jemn04	2021.204	2022.227	−1.023	27.99 (0.25)	0.31	0.92	27.87 (0.12)	0.44	3.23
V178	36634	260.9055490	65.8651822	jeexa4	jemn04	2021.204	2022.227	−1.023	28.71 (0.46)	−0.79	1.29	28.20 (0.17)	0.62	3.25
V179	24684	260.9077303	65.7505134	jeex03	jeex08	2021.035	2021.344	−0.309	27.63 (0.20)	0.76	2.75	27.82 (0.11)	0.27	2.12
V180	26527	260.9094296	65.7355841	jeex03	jeex08	2021.035	2021.344	−0.309	26.13 (0.07)	0.19	2.07	25.04 (0.03)	0.08	2.58

Table 5
(Continued)

ID	CatID	R.A. (deg)	Decl. (deg)	Visit 1	Visit 2	t_1 (yr)	t_2 (yr)	Δt (yr)	$m_{0.24}$ (mag)	$\Delta m_{0.24}$ (mag)	$\sigma_{\Delta m}$	$m_{0.24}$ (mag)	$\Delta m_{0.24}$ (mag)	$\sigma_{\Delta m}$
(1)	(2)	(3)	(4)	(5)	(6)	(7)	(8)	(9)	(10)	(11)	(12)	(13)	(14)	(15)
V181	37131	260.9097335	65.8596199	jeexa4	jemn04	2021.204	2022.227	−1.023	28.03 (0.30)	−1.04	2.53	28.20 (0.15)	−0.48	2.72
V182	36713	260.9145485	65.8642884	jeexa4	jemn04	2021.204	2022.227	−1.023	29.00 (0.85)	0.78	0.68	27.94 (0.14)	0.52	3.23
V183	35903	260.9149584	65.8265971	jeexa4	jdkq05	2021.204	2018.363	2.841	25.20 (0.04)	−0.04	0.62	23.07 (0.01)	0.06	4.82
V184	47170	260.9280848	65.8129725	jemn03	jeexa4	2022.085	2021.204	0.881	27.47 (0.16)	0.54	2.49	27.08 (0.08)	0.21	2.45
V185	37073	260.9288557	65.8578725	jeexa4	jemn04	2021.204	2022.227	−1.023	27.19 (0.15)	−0.63	3.12	27.47 (0.09)	−0.05	0.48
V186	36333	260.9330472	65.8683621	jeexa4	jemn04	2021.204	2022.227	−1.023	24.58 (0.03)	−0.09	2.41	24.65 (0.02)	−0.06	2.32
V187	37009	260.9354158	65.8606655	jeexa4	jemn04	2021.204	2022.227	−1.023	27.68 (0.30)	−1.30	3.17	28.08 (0.15)	−0.43	2.47
V188	36313	260.9427395	65.8689954	jeexa4	jemn04	2021.204	2022.227	−1.023	27.81 (0.24)	−0.83	2.55	27.66 (0.10)	−0.26	2.20
V189	36623	260.9429745	65.8653180	jeexa4	jemn04	2021.204	2022.227	−1.023	27.51 (0.24)	−1.14	3.57	27.59 (0.10)	0.18	1.62
V190	36449	260.9444992	65.8672901	jeexa4	jemn04	2021.204	2022.227	−1.023	28.37 (0.40)	−1.01	1.86	28.62 (0.34)	1.22	3.11

Note. Columns (1)−(9) list the variable source ID, an internal SExtractor catalog ID, the celestial coordinates (determined by SExtractor for the position corresponding to $m_{0.24}$) of the variable source in decimal degrees, the root names of the overlapping visits in which the variable source was detected (Visit 1 and Visit 2), the corresponding UT dates of observation, and the time interval Δt between Visits 1 and 2. Columns (10)−(12) list for the F435W filter the brightest $m_{0.24}$ of the two visits (with the magnitude uncertainty given in parentheses), the change in brightness ($\Delta m_{0.24}$, using the same definition as in Figure 3) between the two visits, and the significance of the variability (σ_{var}). Columns (13)−(15) list the same as Columns (10)−(12), but for the F606W filter.

(This table is available in its entirety in machine-readable form.)

5.4. Caveats

It is important to note that with HST data alone, distinguishing between variability caused by variable AGNs and that caused by faint SNe is challenging. Variability at locations offset from the cores of galaxies could potentially indicate SN events or SMBHs that have not yet reached the galaxy center. In all four catalogs, we identify a total of 25 cases showing variability at locations other than the core, as identified through visual inspection. Identifying AGNs will require complementing this work with ancillary observations of the field to determine whether galaxies exhibiting variability also emit mid-IR emission. Prolonged monitoring of variable objects within this field will contribute to a deeper understanding of SMBHs within galaxies, including their evolution over time and their influence on galactic physics.

We also note that the variable candidates presented here are a *strict lower bound* to the number present in the field: many genuine variable sources, even if at $z \lesssim 6$ and detectable in F606W, were certainly missed because they did not vary sufficiently between specific individual visits to meet our $3\sigma_{\Delta m}$ threshold, or if the timescale of their variability exceeded the duration of the TREASUREHUNT program. In the present study, the photometric uncertainties in each epoch of observation contributed equally to that $3\sigma_{\Delta m}$ threshold. Any future additional observations to similar depths would reduce the photometric uncertainty in the reference magnitudes, thus lowering the variability detection threshold. The magnitude and level of variability for all sources in this work are collected in Table 5, so that they can be compared in future studies within the JWST NEP TDF.

Although significant (i.e., $>3\sigma_{\Delta m}$) direct detections of variability to such exceeding faint limits through systematic monitoring campaigns with HST, JWST, or Roman would require a very large community investment, it is not outside the realm of what is possible. Even at slightly shallower depths, and employing similar extrapolations, variability could account for a large fraction of all accreting SMBHs.

6. Conclusion

This study highlights the JWST NEP TDF as an exceptional site for investigating time-variable astronomical phenomena, including SNe and (weak) variable AGNs. We identified 12 transients and $\sim$100 variable sources in ACS/WFC F606W and F435W images from the HST TREASUREHUNT program. We provide positional information, dates of observation and intervening time interval, and magnitudes for each of the 12 transients, which range in brightness from $\sim$24.8 to $\sim$27.5 mag. Their areal density is $\sim$0.07 transients arcmin^{-2} ($\sim$245 deg^{-2}) per epoch. We argue that the vast majority of these transients are SNe. Three transients (T7, T10, and T11) were detected in X-rays, of which two (T7 and T10) appear isolated and pointlike and are likely newly identified quasars. Transient T11 has no visible host galaxy, and its nature remains uncertain. We suspect it to be a faint quasar if the X-ray detection is indeed associated, or otherwise either part of a very faint dwarf galaxy at $z \lesssim 6$ or a transient in a more massive host at $z \gtrsim 6$. One transient (T4) has a spectroscopic redshift $z = 0.615$ from MMT/Binospec.

Our variability search revealed that 0.42% of the general $z \lesssim 6$ field galaxy population exhibits variability at $\gtrsim 3\sigma_{\Delta m}$ significance to depths of 29.5 mag in F606W and 28.6 mag in

F435W, with an areal density of $\sim$1.25 variables arcmin^{-2} ($\sim$4500 deg^{-2}). We carefully identified variable candidates, using the measured distribution of magnitude differences for objects observed more than once to calibrate our photometric uncertainties, where the scaled photometric uncertainty is $\sigma_{\Delta m}$, as defined in Equation (1). Sources are flagged as variable if they varied by more than $3\sigma_{\Delta m}$ in F435W or F606W or varied by more than $2\sigma_{\Delta m}$ in both filters in the same sense. This revealed 190 unique variable candidates, of which we estimated $\sim$80 to be false positives (using Gaussian statistics). Most of the variable candidates are coincident with the cores of galaxies, indicating potential AGN variability, while a smaller fraction appears to be associated with faint SNe. We also estimate photometric redshifts for our sample, from which we estimate masses, ages, dust extinction, and sSFRs. We briefly explore ways to estimate SMBH mass and AGN timescales using the time interval between overlapping visits and the observed rates of variability.

In conclusion, this work firmly establishes the JWST NEP TDF as a pivotal field for time-domain science with an initial harvest of transients and galaxies exhibiting variability. We emphasize the ability to identify AGNs through their variability in the JWST NEP TDF. Future follow-up observations with HST or JWST could greatly increase the numbers of directly detected variables and to lower variability amplitudes.

Appendix
Assessment of the Potential Impact of Cosmic Rays on Detected Variability

For variability searches with the two HST cameras—WFC3 and ACS—that have been in the telescope for over 15–20 yr it is prudent to consider the number of CRs that will have hit our detectors and may have survived the CR clipping that happens during the drizzling process.

First, we consider how constant the CR flux may be on HST's detectors. A summary of the best on-orbit data on the CR flux is given by, e.g., Ryon (2019, their Section 7.5) for ACS,[46] by Dressel (2016, their Section 5.4.10) for WFC3,[47] and by McMaster & Biretta (2010, their Section 4.9) for WFPC2.[48] Section 4.9 of McMaster & Biretta (2010) suggests that the

---

[46] See also https://www.stsci.edu/files/live/sites/www/files/home/hst/documentation/_documents/acs/acs_ihb_cycle28.pdf.

[47] See also https://www.stsci.edu/files/live/sites/www/files/home/hst/documentation/_documents/wfc3/wfc3_ihb_cycle24.pdf.

[48] See also https://www.stsci.edu/files/live/sites/www/files/home/hst/documentation/_documents/wfpc2/wfpc2_ihb_cycle17.pdf and https://www.stsci.edu/files/live/sites/www/files/home/hst/documentation/_documents/wfpc2/wfpc2_dhb_v5.pdf.

WFPC2 CR energy distribution follows a Weibull distribution, which resembles a Poisson curve with a distinct low-energy cutoff.

A good recent summary of over 1.2 billion CRs analyzed during the 30 yr operational lifetime of these four cameras inside HST is given by, e.g., Miles et al. (2021). Their Table 6 shows that ACS, WFPC2, and WFC3 have remarkably similar densities of CR hits of $\sim 1.1 \pm 0.1$ hits s^{-1} cm^{-2} of detector area. Miles et al. (2021) provide a better physically motivated Landau distribution of the CR energies for all HST cameras, which resembles the earlier Weibull distribution of McMaster & Biretta (2010). These CR energy distributions are thus representative of the typical CR distribution and frequency in typical HST images, as long as one stays away from transitions through the South Atlantic Anomaly (SAA), where the CR flux can be temporarily much higher. Our NEP TDF images always avoid the SAA transitions; therefore, we will assume that the CR flux is as given in these respective Instrument Handbooks and Miles et al. (2021). Following the Instrument Handbooks, at minimum four independent exposures of ~ 1200 s are needed to minimize multiple CR impacts on the same object, and we use a much more conservative $N = 8$ exposures per pointing in each filter. Windhorst et al. (1994) investigate from 12-exposure pointings how much the CR rejection improves if fewer than $N = 12$ exposures are stacked, and they find that for $N = 8$ the sky mean and sky sigma converge to the best achievable values (from the $N = 12$ maximum exposure case) if one clips at the level of 3σ–3.5σ, where σ is the local sky rms noise level. So starting with CR clipping on eight exposures for every pointing should be robust.

Nonetheless, we cannot rule out that the CR flux may occasionally be considerably higher than average, and so we must account for the possibility that, even while using $N = 8$ exposures for each pointing in each filter, some CRs may have survived the clipping procedure upon drizzling and mimic variable objects at the 3.0σ level. For this reason, we also performed additional tests, as described below.

CRs are flagged in the Data Quality extension of ACS images with values of 4096 and 8192. For every variable object, we create a 8×8 pixel box at the center of the measurement, corresponding closely to the 8 pixel diameter aperture used to identify variability (see Section 3.2). We count the number of pixels within this box that may be affected by residual CR flux. We define CR-affected pixels to be those where a CR appears in that exact location in at least half of the stacked exposures (four or more exposures). The location is determined by the WCS in the image header of each individual exposure. For every object, we do this for both epochs and compare the number of CRs in the two epochs. A source is determined to be CR affected if it has at least one CR-affected pixel within the 8×8 pixel box in either epoch. A CR-affected source, as defined here, *may* be affected by CRs, although it is likely not due to the stacking of eight individual exposures with AstroDrizzle.

In Figure 10, we plot the measured change in flux of the objects (between two epochs) versus the combined number of CR-affected pixels. We also plot the difference in the number of pixels affected by CRs between the two epochs, because if one epoch has significantly more CR-affected pixels, this could cause artificial variability. The exercise demonstrates that CRs do not affect our variability detections because the measured flux difference does not depend on the number of

Figure 10. We analyze the potential effect of CRs on the measured flux difference of variable objects in an 8×8 pixel ($0\farcs24 \times 0\farcs24$) area centered on each object. A pixel is considered at risk of CR contamination if it encounters a CR in four or more contributing exposures. Plotted is a random selection of 10,000 galaxies (represented by black points), with median values indicated by green boxes. Left: the absolute value of the difference in measured F606W flux vs. the total number of pixels (in Visit 1 + Visit 2) possibly impacted by CRs. The red shaded region shows objects that are removed for containing too many CRs. The y-axis is logarithmically scaled except between -0.1 and 0.1, which is scaled linearly. The x-axis is linearly scaled up to 20, where it is then logarithmically scaled to 50. Right: the absolute value of the difference in measured F606W flux vs. the difference in the number of pixels potentially affected by CRs.
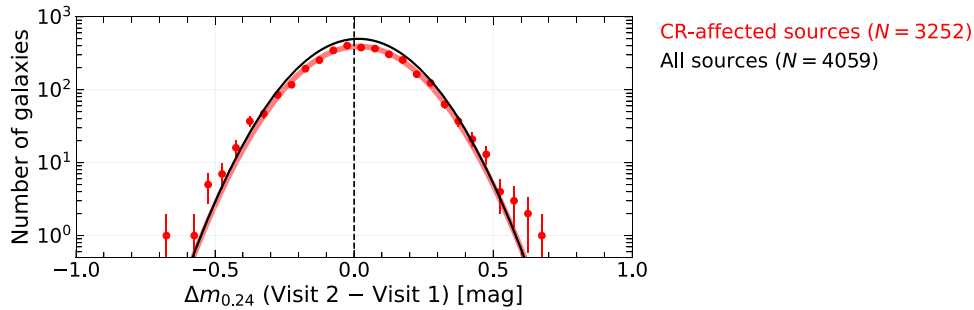
Figure 11. Histogram of the distribution of magnitudes differences measured between two epochs ($\Delta m_{0.24}$) for 4059 galaxies between 28.0 mag $< m_{AB} < 28.5$ mag. We compare the sample of CR-affected galaxies (red) to the full sample (black). The points show the fraction of CR-affected galaxies (N) for each $\Delta m_{0.24}$ bin, where the error bar is $\sqrt{N}$. The solid lines are Gaussian fits to the data. The black solid line represents the Gaussian fit to the full sample. Our empirical uncertainties estimated in Figure 3 already account for CR effects, as shown by the black line closely following the red line.

CR-affected pixels or the difference in the number of CR-affected pixels. Moreover, ~31% of the 10,000 galaxies sampled in Figure 10 have zero CR-affected pixels in both epochs.

One object with very high measured differences in flux also has a large number of pixels with CRs. We opt to reject and remove two objects with more than 25 pixels (~25% of the pixels in the aperture) by CRs. There were no variable candidates that met this criterion.
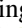
We also confirm that the distribution of $\Delta m_{0.24}$ is Gaussian for sources potentially affected by CRs, shown in Figure 11. More importantly, since a majority (~80%) of sources in our data set are potentially affected by CRs, our empirical uncertainties in Section 3.2.2 already account for CR effects. This is specifically represented by the fact that the Gaussian fit to the CR-affected sources (red line) is within 0.01 mag of the Gaussian fit for the full data (black line). The latter (black line) was used to calibrate our empirical uncertainties in Section 3.2.2. We note that, by eye, there appears to be a slight divergence from the Gaussian fit at $\sigma_{\Delta m} < -0.5$ and $\sigma_{\Delta m} > 0.5$. However, only the outermost points seem to contribute to this trend, corresponding to fewer than five sources (or less than 0.2% of sources).

In conclusion, this evidence suggests that CRs rarely appear in the final drizzled images. The spurious transients (in

Section 3.1) were likely outliers, and any other spurious CRs to this degree would have been identified during the transient search. In addition, if CRs affect the brightness of sources regularly, our empirical estimation of uncertainties in Section 3.2.2 already accounts for this. Nonetheless, we do not completely eliminate the possibility that some (albeit very few) of our variable candidates may be affected by CRs that cause artificial variability. In other words, although we assume that a majority of our sources are not affected by CRs, follow-up observations remain necessary to confirm which sources are truly variable, as well as to reveal other sources that were missed in this work.

ORCID iDs

Rosalia O'Brien ⓘ https://orcid.org/0000-0003-3351-0878
Rolf A. Jansen ⓘ https://orcid.org/0000-0003-1268-5230
Norman A. Grogin ⓘ https://orcid.org/0000-0001-9440-8872
Seth H. Cohen ⓘ https://orcid.org/0000-0003-3329-1337
Brent M. Smith ⓘ https://orcid.org/0000-0002-0648-1699
Ross M. Silver ⓘ https://orcid.org/0000-0001-6564-0517
W. P. Maksym, III ⓘ https://orcid.org/0000-0002-2203-7889
Rogier A. Windhorst ⓘ https://orcid.org/0000-0001-8156-6281
Timothy Carleton ⓘ https://orcid.org/0000-0001-6650-2853
Anton M. Koekemoer ⓘ https://orcid.org/0000-0002-6610-2048

Nimish P. Hathi https://orcid.org/0000-0001-6145-5090
Christopher N. A. Willmer https://orcid.org/0000-0001-9262-9997
Brenda L. Frye https://orcid.org/0000-0003-1625-8009
M. Alpaslan https://orcid.org/0000-0003-0321-1033
M. L. N. Ashby https://orcid.org/0000-0002-3993-0745
T. A. Ashcraft https://orcid.org/0000-0003-4439-6003
N. Cappelluti https://orcid.org/0000-0002-1697-186X
F. Civano https://orcid.org/0000-0002-2115-1137
C. J. Conselice https://orcid.org/0000-0003-1949-7638
V. S. Dhillon https://orcid.org/0000-0003-4236-9642
S. P. Driver https://orcid.org/0000-0001-9491-7327
K. J. Duncan https://orcid.org/0000-0001-6889-8388
M. Elvis https://orcid.org/0000-0001-5060-1398
G. G. Fazio https://orcid.org/0000-0002-0670-0708
S. L. Finkelstein https://orcid.org/0000-0001-8519-1130
H. B. Gim https://orcid.org/0000-0003-1436-7658
A. Griffiths https://orcid.org/0000-0003-1880-3509
H. B. Hammel https://orcid.org/0000-0001-8751-3463
M. Hyun https://orcid.org/0000-0003-4738-4251
M. Im https://orcid.org/0000-0002-8537-6714
V. R. Jones https://orcid.org/0000-0003-4665-8521
D. Kim https://orcid.org/0000-0001-5120-0158
R. L. Larson https://orcid.org/0000-0003-2366-8858
S. Malhotra https://orcid.org/0000-0002-9226-5350
M. A. Marshall https://orcid.org/0000-0001-6434-7845
S. N. Milam https://orcid.org/0000-0001-7694-4129
J. D. R. Pierel https://orcid.org/0000-0002-2361-7201
J. E. Rhoads https://orcid.org/0000-0002-1501-454X
S. A. Rodney https://orcid.org/0000-0003-1947-687X
H. J. A. Röttgering https://orcid.org/0000-0001-8887-2257
M. J. Rutkowski https://orcid.org/0000-0003-3527-1428
R. E. Ryan, Jr. https://orcid.org/0000-0003-0894-1588
M. J. Ward https://orcid.org/0000-0003-1810-0889
C. W. White https://orcid.org/0000-0002-0486-0222
R. J. van Weeren https://orcid.org/0000-0002-0587-1660
X. Zhao https://orcid.org/0000-0002-7791-3671
J. Summers https://orcid.org/0000-0002-7265-7920
J. C. J. D'Silva https://orcid.org/0000-0002-9816-1931
R. Ortiz, III https://orcid.org/0000-0002-6150-833X
A. S. G. Robotham https://orcid.org/0000-0003-0429-3579
D. Coe https://orcid.org/0000-0001-7410-7669
M. Nonino https://orcid.org/0000-0001-6342-9662
N. Pirzkal https://orcid.org/0000-0003-3382-5941
H. Yan https://orcid.org/0000-0001-7592-7714

References

Astropy Collaboration, Price-Whelan, A. M., Lim, P. L., et al. 2022, ApJ, 935, 167
Astropy Collaboration, Price-Whelan, A. M., Sipőcz, B. M., et al. 2018, AJ, 156, 123
Astropy Collaboration, Robitaille, T. P., & Tollerud, E. J. 2013, A&A, 558, A33
Bertin, E., & Arnouts, S. 1996, A&AS, 117, 393
Blanc, G. A., Lira, P., Barrientos, L. F., et al. 2008, ApJ, 681, 1099
Bohlin, R. C., Ryon, J. E., & Anderson, J. 2020, Update of the Photometric Calibration of the ACS CCD Cameras, Instrument Science Report ACS 2020-8, (Baltimore, MD: STScI)
Boquien, M., Burgarella, D., Roehlly, Y., et al. 2019, A&A, 622, A103
Boutsia, K., Leibundgut, B., Trevese, D., & Vagnetti, F. 2009, A&A, 497, 81
Bradley, L., Sipőcz, B., Robitaille, T., et al. 2022, astropy/photutils: v1.5.0, Zenodo, doi:10.5281/zenodo.6825092
Brammer, G. B., van Dokkum, P. G., & Coppi, P. 2008, ApJ, 686, 1503
Bruzual, G., & Charlot, S. 2003, MNRAS, 344, 1000
Burke, C. J., Shen, Y., Blaes, O., et al. 2021, Sci, 373, 789

Calzetti, D., Armus, L., Bohlin, R. C., et al. 2000, ApJ, 533, 682
Cappellaro, E. 2014, in IAU Symp. 296, Supernova Environmental Impacts, ed. A. Ray & R. A. McCray (Cambridge: Cambridge Univ. Press), 37
Cappellaro, E., Botticella, M. T., Pignata, G., et al. 2015, A&A, 584, A62
Casertano, S., de Mello, D., Dickinson, M., et al. 2000, AJ, 120, 2747
Chakrabarti, S., Dell, B., Graur, O., et al. 2018, ApJL, 863, L1
Chambers, K. C., Magnier, E. A., Metcalfe, N., et al. 2016, arXiv:1612.05560
Ciesla, L., Elbaz, D., & Fensch, J. 2017, A&A, 608, A41
Cohen, S. H., Ryan, R. E., & Straughn, J. 2006, ApJ, 639, 731
Cristiani, S., Trentini, S., La Franca, F., & Andreani, P. 1997, A&A, 321, 123
Cristiani, S., Vio, R., & Andreani, P. 1990, AJ, 100, 56
Dahlen, T., Strolger, L.-G., Riess, A. G., et al. 2012, ApJ, 757, 70
Dale, D. A., Helou, G., Magdis, G. E., et al. 2014, ApJ, 784, 83
Dressel, L. 2016, WFC3 Instrument Handbook for Cycle 24, v8 (Baltimore, MD: STScI)
Fabricant, D., Fata, R., Epps, H., et al. 2019, PASP, 131, 075004
Ferrarese, L., & Merritt, D. 2000, ApJL, 539, L9
Fruchter, A. S., Hack, W., Droetboom, M., et al. 2009, AAS Meeting, 213, 467.02
Fruscione, A., McDowell, J. C., Allen, G. E., et al. 2006, Proc. SPIE, 6270, 62701V
Gaia Collaboration, Prusti, T., de Bruijne, J. H. J., et al. 2016, A&A, 595, A1
Gaia Collaboration, Vallenari, A., Brown, A. G. A., et al. 2023, A&A, 674, A1
Gebhardt, K., Bender, R., Bower, G., et al. 2000, ApJL, 539, L13
Giveon, U., Maoz, D., Kaspi, S., Netzer, H., & Smith, P. S. 1999, MNRAS, 306, 637
Graur, O., Rodney, S. A., Maoz, D., et al. 2014, ApJ, 783, 28
Hoffmann, S. L., Mack, J., Avila, R., et al. 2021, AAS Meeting, 53, 216.02
Hook, I. M., McMahon, R. G., Boyle, B. J., & Irwin, M. J. 1994, MNRAS, 268, 305
Jakobsen, P., Jansen, R. A., Wagner, S., & Reimers, D. 2003, A&A, 397, 891
Jansen, R. A., & Windhorst, R. A. 2018, PASP, 130, 124001
Joye, W. A., & Mandel, E. 2003, in ASP Conf. Ser. 295, Astronomical Data Analysis Software and Systems XII, ed. H. E. Payne, R. I. Jedrzejewski, & R. N. Hook (San Francisco, CA: ASP), 489
Kawaguchi, T., & Mineshige, S. 1999, in IAU Symp. 194, Activity in Galaxies and Related Phenomena, ed. Y. Terzian, E. Khachikian, & D. Weedman (San Francisco, CA: ASP), 356
Koekemoer, A. M., Fruchter, A. S., Hook, R. N., & Hack, W. 2003, The 2002 HST Calibration Workshop: Hubble after the Installation of the ACS and the NICMOS Cooling System, ed. S. Arribas, A. Koekemoer, & B. Whitmore, (Baltimore, MD: STScI), 337
Kormendy, J., & Ho, L. C. 2013, ARA&A, 51, 511
Kurtz, M. J., Eichhorn, G., Accomazzi, A., et al. 2000, A&AS, 143, 41
Labbé, I., Franx, M., Rudnick, G., et al. 2003, AJ, 125, 1107
Li, S.-L., & Cao, X. 2008, MNRAS, 387, L41
Lynden-Bell, D. 1969, Natur, 223, 690
Lyu, J., Alberts, S., Rieke, G. H., & Rujopakarn, W. 2022, ApJ, 941, 191
Lyu, J., Alberts, S., Rieke, G. H., et al. 2023, arXiv:2310.12330
Lyu, J., & Rieke, G. 2022, Univ, 8, 304
Magorrian, J., Tremaine, S., Richstone, D., et al. 1998, AJ, 115, 2285
Matteucci, F., & Greggio, L. 1986, A&A, 154, 279
McMaster, M., & Biretta, J. 2010, WFPC2 Standard Star CTE, Instrument Science Report 2010-01, (Baltimore, MD: STScI)
Meinke, J., Böckmann, K., Cohen, S., et al. 2021, ApJ, 913, 88
Meinke, J., Böckmann, K., Cohen, S., et al. 2023, ApJ, 952, 170
Miles, D., Deustua, S. E., Tancredi, G., et al. 2021, ApJ, 918, 86
Mink, D. J. 2002, in ASP Conf. Ser. 281, Astronomical Data Analysis Software and Systems XI, ed. D. A. Bohlender, D. Durand, & T. H. Handley (San Francisco, CA: ASP), 169
Mink, J., 2011 WCSTools: Image Astrometry Toolkit, Astrophysics Source Code Library, ascl:1109.015
Morokuma, T., Doi, M., Yasuda, N., et al. 2008, ApJ, 676, 163
O'Brien, R., Carleton, T., Windhorst, R. A., et al. 2023, AJ, 165, 237
Oke, J. B., & Gunn, J. E. 1983, ApJ, 266, 713
Papovich, C., Shipley, H. V., Mehrtens, N., et al. 2016, ApJS, 224, 28
Planck Collaboration, Ade, P. A. R., Aghanim, N., et al. 2016, A&A, 594, A13
Planck Collaboration, Aghanim, N., Akrami, Y., et al. 2020, A&A, 641, A6
Pouliasis, E., Georgantopoulos, I., Bonanos, A. Z., et al. 2019, MNRAS, 487, 4285
Rawes, J., Worrall, D. M., & Birkinshaw, M. 2015, MNRAS, 452, 3064
Reines, A. E., Condon, J. J., Darling, J., & Greene, J. E. 2020, ApJ, 888, 36
Riess, A. G., Anand, G. S., Yuan, W., et al. 2023, ApJL, 956, L18
Riess, A. G., Filippenko, A. V., Challis, P., et al. 1998, AJ, 116, 1009
Robotham, A. S. G., D'Silva, J. C. J., Windhorst, R. A., et al. 2023, PASP, 135, 085003

Rodney, S. A., Riess, A. G., Strolger, L.-G., et al. 2014, AJ, 148, 13

Ryon, J. E. 2019, Advanced Camera for Surveys Instrument Handbook for Cycle 27, v18.0 (Baltimore, MD: STScI)

Sarajedini, V. L., Gilliland, R. L., & Kasm, C. 2003, ApJ, 599, 173

Sarajedini, V. L., Koo, D. C., Klesman, A. J., et al. 2011, ApJ, 731, 97

Shakura, N. I., & Sunyaev, R. A. 1976, MNRAS, 175, 613

Smith, B. M., Windhorst, R. A., Cohen, S. H., et al. 2020, ApJ, 897, 41

Smith, B. M., Windhorst, R. A., Jansen, R. A., et al. 2018, ApJ, 853, 191

Smith, B. M., Windhorst, R. A., Teplitz, H., et al. 2024, ApJ, 964, 73

Sokolovsky, K. V., Gavras, P., Karampelas, A., et al. 2017, MNRAS, 464, 274

Trevese, D., Kron, R. G., Majewski, S. R., Bershady, M. A., & Koo, D. C. 1994, ApJ, 433, 494

Ulrich, M.-H., Maraschi, L., & Urry, C. M. 1997, ARA&A, 35, 445

Vanden Berk, D. E., Wilhite, B. C., Kron, R. G., et al. 2004, ApJ, 601, 692

Villforth, C., Koekemoer, A. M., & Grogin, N. A. 2010, ApJ, 723, 737

Villforth, C., Sarajedini, V., & Koekemoer, A. 2012, MNRAS, 426, 360

Whitaker, K. E., Labbé, I., van Dokkum, P. G., et al. 2011, ApJ, 735, 86

Wilhite, B. C., Brunner, R. J., Grier, C. J., Schneider, D. P., & vanden Berk, D. E. 2008, MNRAS, 383, 1232

Windhorst, R. A., Cohen, S. H., Hathi, N. P., et al. 2011, ApJS, 193, 27

Windhorst, R. A., Cohen, S. H., Jansen, R. A., et al. 2023, AJ, 165, 13

Windhorst, R. A., Franklin, B. E., & Neuschaefer, L. W. 1994, PASP, 106, 798

Wold, M., Brotherton, M. S., & Shang, Z. 2007, MNRAS, 375, 989

Xie, G.-Z., Chen, L.-E., Li, H.-Z., et al. 2005, ChJAA, 5, 463

Zhao, X., Civano, F., Fornasini, F. M., et al. 2021a, yCat, J/MNRAS/508/5176

Zhao, X., Civano, F., Fornasini, F. M., et al. 2021b, MNRAS, 508, 5176

Zhao, X., Civano, F., Willmer, C. N. A., et al. 2024, ApJ, 965, 188

Zhong, Y., Inoue, A. K., Yamanaka, S., & Yamada, T. 2022, ApJ, 925, 157

Zuo, W., Wu, X.-B., Liu, Y.-Q., & Jiao, C.-L. 2012, ApJ, 758, 104